A constitutive model for a rate and temperature-dependent, plastically anisotropic titanium alloy

Miguel Ruiz de Sotto, Patrice Longère, Véronique Doquet, Jessica Papasidero

A constitutive model for a rate and temperature-dependent, plastically anisotropic titanium alloy

Miguel Ruiz de Sotto[a,b,c], Patrice Longère[a,*], Véronique Doquet[b], Jessica Papasidero[c]

[a] *ICA, Université de Toulouse, ISAE-SUPAERO, MINES ALBI, UPS, INSA, CNRS, 31000 Toulouse, France*
[b] *Laboratoire de Mécanique des Solides, CNRS UMR 7649, Ecole Polytechnique, 91128 Palaiseau, France*
[c] *Safran Aircraft Engines, Rond point René Ravaud, 77550 Réau, France*

Abstract

Aircraft engine fan blades are notably designed to withstand impact loading involving large deformation, high strain rate, non-proportional loading paths and self-heating. Due to their high strength-to-weight ratio and good toughness, Ti-6Al-4V titanium alloys are promising candidates for the blades leading edge. An extensive experimental campaign on a Ti-6Al-4V titanium alloy provided in the form of cold rolled plates has been carried out. The thermo-mechanical characterization consisted in tension, compression and shear tests performed at various strain rates and temperatures, and under monotonic as well as alternate loading paths. A constitutive model has been accordingly developed accounting for the combined effect of plastic orthotropy and tension/compression asymmetry, nonlinear isotropic and kinematic strain hardening, strain rate hardening, and thermal softening. The constitutive model has been implemented as a user material subroutine into the commercial finite element computation code LS-DYNA. The performances of the model have been estimated by conducting numerical simulations considering a volume element under various loading paths as well as the specimens used for the experimental campaign.

*Corresponding author
Email address: Patrice.LONGERE@isae-supaero.fr (Patrice Longère)

Keywords: titanium alloy, plastic anisotropy, dynamic plasticity, complex loading, numerical simulation
2019 MSC: 00-01, 99-00

1. Introduction

In the certification of aircraft engines regarding accidental events, real scale ballistic tests including bird strike or fan blade loss must be passed without compromising the engine performance. During such tests the fan blades undergo large deformation, high strain rate, non-proportional multi-axial loading, load reversals and self-heating until potential fracture. In the numerical simulation-aided design of impact-resistant fan blades, a constitutive model able to account for all these parameters is thus needed. This work focuses on Ti-6Al-4V titanium alloys known for their high strength-to-weight ratio and good toughness [1] and accordingly considered as promising candidates for the leading edge of multi-component fan blades.

Ti-6Al-4V is a quasi-α titanium alloy which can have various microstructures, among which the bimodal form considered here, consisting of relatively "soft" primary α phase nodules with an hexagonal close packed (HCP) crystallography within a harder body centered cubic (BCC) β matrix containing tiny secondary α laths. Both dislocation glide and mechanical twinning (mostly of the tensile $\{10\bar{1}2\}(\bar{1}011)$ type) are activated in Ti-6Al-4V upon plastic deformation, as reported by Prakash and Coghe et al [2, 3]. Cold rolled plates of a Ti-6Al-4V titanium alloy usually exhibit a strong texture [4]. As reported in Lee et al. [5], primary α grains usually tend to rotate so that their $\langle 0001 \rangle$ direction becomes perpendicular to the rolling direction. An orthotropic behavior can thus be observed with a significantly different yield strength along the rolling, transverse and normal directions of the plate. Hill's criterion [6] has been widely used to model the plastic behaviour of orthotropic materials due to its simplicity [7–9]. It consists in incorporating a fourth order tensor in the equivalent stress in order to make the yield stress dependent on the orientation.

Plastic anisotropy evolving with strain has also been addressed by Baltov and Sawcsuk [10] by defining the fourth order tensor as a polynomial decomposition of notably the strain invariants [11]. Karafillis and Boyce [12] proposed a linear transformation of the stress tensor itself to induce orthotropy in plastic yielding without compromising the convexity of the yield function [13]. Some examples of this strategy can be seen in [14–18]. Moreover, a generalized version of the Karafillis and Boyce yield surface was later proposed by Bron and Besson [19] to improve the description of plastic anisotropy.

The strength differential between tension and compression often observed in titanium alloys and other HCP metals is generally ascribed to the different activation of $\langle c+a\rangle\{11\bar{2}2\}\langle 11\bar{2}3\rangle$ slip systems [20] and mechanical twinning [2, 21] depending on the loading direction. To model this effect, some authors have proposed asymmetric yield criteria including the third invariant of the stress tensor [22, 23]. Khan et al. proposed a criterion that manages to independently include the orthotropy, by means of the Hill criterion, and the asymmetry, by introducing a function depending on the Lode parameter [24]. With this method, the strength differential is successfully captured with only one material coefficient. Similarly, the CPB06 yield criterion [25] can simultaneously capture the orthotropy and the strength differential by combining a linear transformation of the stress deviator tensor and a yield function of the principal stresses. The simplicity, applicability and accuracy of this last model has made it widely used as seen in [26–28]. Furthermore, distortional models such as the Homogeneous yield function-based Anisotropic Hardening (HAH) model [29] has been proven useful when considering an evolving anisotropy that continuously distorts and rotates the yield surface as it was later on successfully applied on titanium [30]. A last example worth mentioning for the modeling of asymmetry was proposed by Longère [31] who included a definition of a viscous stress dependent on the hydrostatic pressure (while maintaining the plastic yield criterion pressure-independent).

Bauschinger effect in the mechanical behavior of metals and alloys has been extensively studied, for example in Zhonghua and Gu [32, 33] for dual-phase steel

or Helbert et al. [34] for titanium alloys. Since ballistic events on fan blades induce load reversals, it is crucial to take kinematic hardening into account in the constitutive modeling of Ti-6Al-4V. A kinematic hardening-related internal variable was introduced in the Prager model to describe this effect [35], nonlinear extensions for the evolution of this variable were later on proposed by Armstrong and Frederick [36] and Chaboche [37]. As kinematic hardening may produce transient effects and permanent softening, mixed coupled hardening models are proposed in the literature to predict such effects [38–40]. Another alternative to reproduce the Bauschinger effect is through the yield surface distortion as it is proposed with the HAH model [29].

The behavior of titanium alloys is known to be strongly strain rate dependent, see e.g. Minaar and Zhou [41] or Tuninetti and Habraken [26]. The engineering-oriented Johnson-Cook constitutive model [42] is widely employed to describe the hardening due to strain rate. Yet, it scarcely fits the experimental behavior of HCP metals and some modifications have been proposed to improve the agreement with experiments, see e.g. Khan et al. [43]. Alternatively, an additive formulation where strain rate and plastic deformation effects are treated separately is also used to model viscoplasticity (see Longère [44]).

The strong temperature-dependence of Ti-6Al-4V titanium alloys is also well-known, see e.g. Seo et al. [45]. Therefore, a thermal softening function is generally considered to describe the decrease of the yield stress with increasing temperature. In addition, due to its low heat capacity, significant self-heating induced temperature rise may occur under adiabatic conditions at high loading rates [46, 47]. Consequently, a competition between strain and strain rate hardening and thermal softening takes place along the deformation process potentially leading to material instability and further strain localization under adiabatic shear banding, see e.g. Longère and Dragon [48].

There is an extensive literature dedicated to modeling the above mentioned effects individually. Yet, scarce are the models that can simultaneously take into account all the features observed in Ti-6Al-4V titanium alloys. For instance, Tancogne-Dejean et al. [49] modeled the orthotropy of a Ti-6Al-4V with a non-

associated plastic law using the Lankford coefficients. However, the strength-differential is not described in their work. Both the effects of orthotropy and strength differential were well modelled in Gilles et al. [4] for a Ti-6Al-4V but at room temperature and within the quasi-static regime. Later on, Tunineti and Habraken [26] used an anisotropic model with an added temperature dependence but it was limited by the strain rate range of the calibration. A more extended investigation was done by Khan et al. [50] where anisotropy, temperature, strain rate as well as multiaxial non-proportional loading were modeled, although no considerations were made regarding the adiabatic conditions at high strain rate. Furthermore, these authors did not include either kinematic hardening necessary to reproduce the load reversals appearing during a ballistic event.

The aim of the present work is to palliate this deficiency by developing an advanced constitutive model able to simultaneously describe all the effects involved during a ballistic event on a structure made of Ti-6Al-4V alloy, namely related to (i) texture-induced loading orientation, (ii) load-reversals as well as non-proportionality, (iii) strain rate and (iv) temperature. Accounting for the salient effects of the underlying micro-mechanisms, a phenomenological approach is developed within the irreversible thermodynamics framework instead of a polycrystalline formalism as proposed by e.g. Zhang et al. [51] or Mayeur and McDowell [52].

The paper is divided in three parts. The first part is dedicated to the experimental characterization of the mechanical behavior under monotonic and cycling loadings at various strain rates and temperatures, as well as stress relaxation tests. The second part presents in detail the constitutive model. The third part is dedicated to the numerical implementation of the model in the commercial finite element computation code LS-DYNA and the evaluation of its performances at the volume element scale and then at the structure scale.

2. Experimental Characterization

The following section summarizes the results of an extensive experimental campaign under a wide range of strain, strain rate, temperature and loading path. The low strain rate (quasi static) tests are performed by using conventional tension-compression testing machines and the high strain rate (dynamic) tests by means of compression and tension split Hopkinson pressure bar (SHPB)-type set-ups. After a brief presentation of the material under consideration, the experimental results are shown and commented in detail.

2.1. Ti-6Al-4V grade under consideration

The Ti-6Al-4V alloy with a bimodal microstructure under consideration is provided in the form of a 16 mm-thick cold-rolled sheet. The size of the equiaxed α phase nodules ranges from a few microns up to 30 µm (see Figure 1a). Figure 1b shows an orientation map for the α phase issued from an EBSD (*Electron Back-Scatter Diffraction*) analysis of the sheet. The observed zone of approximately $3\,\mathrm{mm}^2$ presents clearly zones with different orientations. These "macro-zones" are inherited from the orientation of the prior β grains formed during previous thermomechanical treatments of the alloy [53], and it produces some scatter in the experimental results since the scale of these zones approaches that of the specimens tested. Even though the texture is locally pronounced, in average the global texture is not very marked, as shown by the pole figures obtained by X-ray diffraction presented in Figure 1c.

2.2. Experimental set-up: low vs. high strain rate

The loading direction-related component ε of the logarithmic strain tensor $\underline{\underline{\varepsilon}}$ is defined as $\varepsilon = ln\,(1+\varepsilon_N)$, where $\varepsilon_N = \frac{\Delta l}{l_0}$ is the nominal strain with Δl the gauge length elongation given by the extensometer and l_0 the initial gauge length. Under the small strain assumption tentatively adopted here, the strain ε is partitioned into elastic ε^e and plastic ε^p contributions, viz. $\varepsilon = \varepsilon^e + \varepsilon^p$, for the uniaxial tests (this assumption is discussed later on in the following section dedicated to constitutive modeling, see section 3.1). The corresponding stress

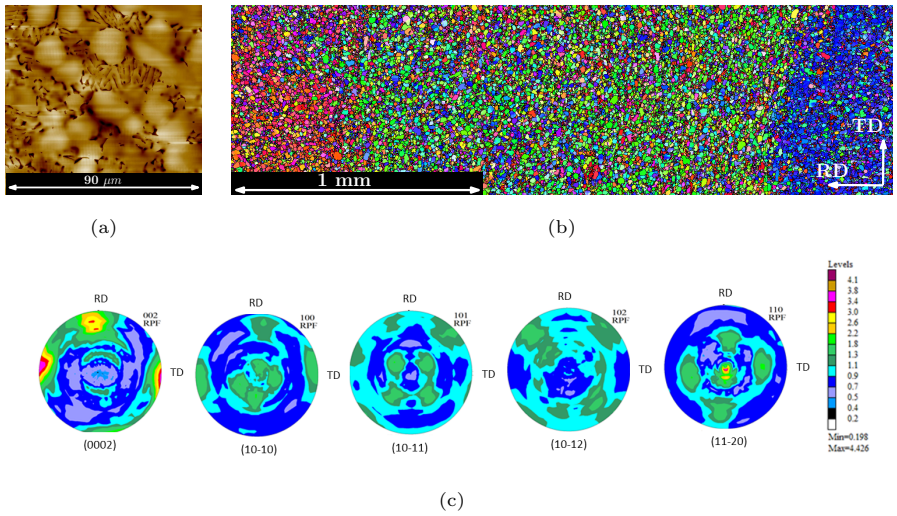

Figure 1: Microstructure of the as-received material in the RD-TD plane a) atomic force microscopy b) α phase orientation map obtained by EBSD and c) pole figures obtained by X-ray diffraction.

component σ of the Cauchy stress tensor $\underline{\underline{\sigma}}$ is given by $\sigma = (F/A) \cdot (1 + \varepsilon_N)$, where F is the load and A the initial cross-section area.

The stress triaxiality ratio χ used in the following is defined as $\chi = -p/\sigma_{vm}$ where p and σ_{vm} represent the pressure and von Mises equivalent stress, respectively, with p=-Tr$\underline{\underline{\sigma}}/3$, $\sigma_{vm} = \sqrt{\frac{3}{2}\underline{\underline{s}} : \underline{\underline{s}}}$, $\underline{\underline{s}} = \underline{\underline{\sigma}} + p\underline{\underline{I}}$ the deviatoric stress tensor, $\underline{\underline{I}}$ being the identity tensor.

Various types of specimens have been machined along four directions: the rolling (RD), transverse (TD) and normal (ND) direction, as well as a diagonal (DD) direction in the RD-TD plane pointing 45° with respect to the rolling direction. Specimens are ranked in Figure 2 according to increasing stress triaxiality ratio χ from left to right.

2.2.1. Low Strain Rate

The tension dog-bone specimen dimensions in Figure 2 for $\chi \simeq 1/3$ are 2 mm × 3 mm × 6 mm (thickness x width x gauge length). A shorter specimen is used for the normal direction (ND) since the dimensions are limited by the sheet

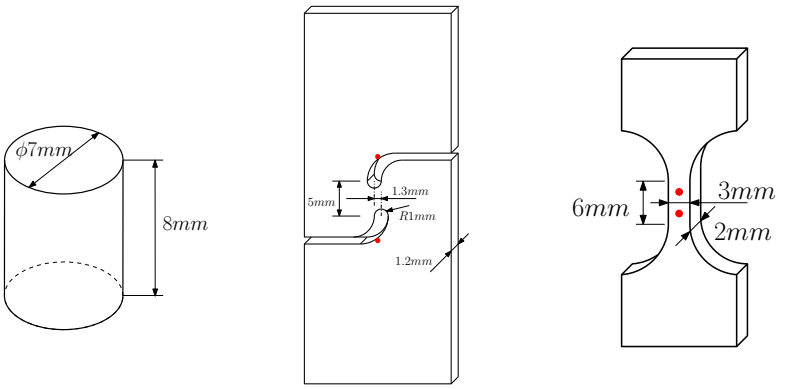

$\chi \simeq -1/3$ (a) Compression. $\chi \simeq 0.0$ (b) Shear. $\chi \simeq 1/3$ (c) Smooth specimen.

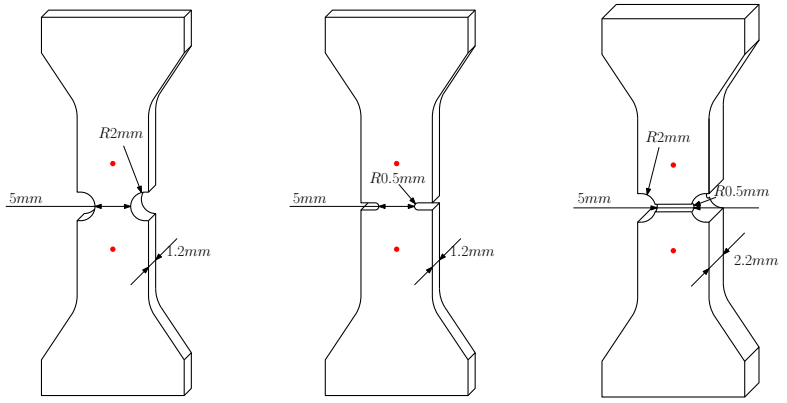

$\chi \simeq 1/2$ (d) Notch of 2 mm. $\chi \simeq 2/3$ (e) Notch of 0.5 mm. $\chi \simeq 1.0$ (f) Double notch.

Figure 2: Specimen geometries and corresponding stress triaxiality ratio χ (determined by preliminary numerical simulations). The nominal strain is measured with a mechanical extensometer of an initial length of 12 mm whose position is indicated with red dots.

160 thickness. Its cross section remains the same, but the gauge length is reduced to 4 mm. For compression ($\chi \simeq -1/3$), cylindrical specimen dimensions are 8 mm × 7 mm (height x diameter). For the cyclic tests, a cylindrical specimen of a radius of 8 mm and a gauge length of 8 mm is employed. Notched shear and tension specimens ($\chi \simeq 0, 1/2, 2/3, 1.0$) have been machined so as to widen

the stress triaxiality ratio range under consideration. Two notch radii of 2 mm and 0.5 mm are employed to reach expected average χ of about 1/2 and 2/3 in tension (according to preliminary finite element simulations, not shown here). In addition, a specimen notched both in width and thickness is used to get a χ close to 1.0. Moreover, in order to get an average χ close to 0, the shear specimen geometry designed by Roth [54] has been used. For the shear specimen, the notches are machined with a constant radius which is suited for medium ductility materials. Additionally, both notches are separated by a slight offset which avoids too severe tensile stresses on the border when largely deformed.

A series of displacement-controlled quasi-static tests are performed along the different orientations under tension and compression loading with strain rates ranging from $|\dot{\varepsilon}| \simeq 10^{-4}\,\mathrm{s}^{-1}$ to $10^{-1}\,\mathrm{s}^{-1}$.

The load is measured by load cells of 10 kN or 100 kN depending on the size of the specimens.

In the case of compression tests at room temperature, an axial clip-on extensometer with 12.5 mm gauge length and +/- 5 mm displacement range is mounted on the rigid plates compressing the sample. Some grease was applied as lubricant on the samples surface in order to minimize the barreling effect. During tension tests as well as under cyclic loadings (and uniaxial compression at high temperature), the strain is measured by tracking marker points on the sample surface. For high temperature tests, an oven reaching temperatures of up to 350 °C is employed. The temperature of the sample is controlled by a thermocouple and does not fluctuate by more than 2 °C around the setpoint during the whole mechanical test. For the tests on shear and notched specimens, the nominal strain is measured by employing a clip-on mechanical extensometer of 12 mm-initial gauge length.

2.2.2. High Strain Rate

Split-Hopkinson pressure bars (SHPB) set-ups are used for compression and tension tests at high strain rates of up to $|\dot{\varepsilon}| \simeq 1.5 \times 10^{3}\,\mathrm{s}^{-1}$, at room temperature. For tension tests, the load-inversion device developed by Dunand et al.

[55] and extended by Roth et al. [56] is used. In order to obtain the desired high loading rate, the tensile specimen is $1.2\,\text{mm} \times 3\,\text{mm} \times 10\,\text{mm}$ (thickness x width x gauge length) and the compression specimen is $4.7\,\text{mm} \times 5.4\,\text{mm}$ (height x diameter).

According to the one-dimensional analysis of the wave propagation in compression tests [57], the specimen strain rate and load transferred to the specimen are measured via strain gauges glued on the input and output bars. In the case of tensile dynamic tests, the force is still measured with a strain gauge on the output bar. The strain field in the sample is obtained by digital image correlation (DIC), based on images captured with a Phanton v7.3 high speed camera. A frame rate of up to $10^5\,\text{Hz}$ with a resolution of $304 \times 64\,\text{px}^2$ is employed to observe the zone of interest of $10 \times 3\,\text{mm}^2$ covered with speckle painting using an airbrush. The VIC-2D software is used for DIC and the mean strain in the gauge length is measured using a virtual extensometer following the relative displacement of two points of the speckle.

2.3. Experimental results

In a first approximation, the uniaxial component σ measured along the loading direction is assumed to be additively decomposed into a kinematic hardening contribution σ_{KH}, an isotropic hardening contribution σ_{IH} and a viscous contribution σ_v which all depend on a finite number of parameters, namely the orientation θ, the triaxiality χ, the temperature T, the accumulated plastic strain κ and the plastic strain rate $\dot{\kappa}$ (in this section, we tentatively assume $\kappa \simeq |\varepsilon^p|$ and $\dot{\kappa} \simeq |\dot{\varepsilon}^p|$ under monotonic uniaxial loading). The stress σ accordingly reads

$$|\sigma| \simeq \sigma_{KH}\left(\theta, \chi, \kappa, T\right) + \sigma_{IH}\left(\theta, \chi, T, \kappa\right) + \sigma_v\left(\dot{\kappa}, \theta, \chi, \kappa, T\right) \tag{1}$$

where the kinematic and isotropic hardening contributions σ_{KH} and σ_{IH} are assumed to be rate independent. The aim is to identify each contribution.

In a first step, the dependence on the loading direction θ, loading path χ, temperature T and strain rate $\dot{\kappa}$ is quantified by an analysis of the total stress $(\sigma_{KH} + \sigma_{IH} + \sigma_v)$. For this purpose, monotonic, cyclic and relaxation

loadings are employed. Secondly, the contributions of the rate independent stress ($\sigma_{KH} + \sigma_{IH}$) and the viscous stress (σ_v) are identified.

For confidentiality reasons, the stress values determined in the following are normalized, viz. $\tilde{\sigma} = \sigma/\sigma_{RD_0}$, where σ_{RD_0} is the yield stress at 0.2 % of plastic strain along the rolling direction at room temperature and $\dot{\varepsilon} \simeq 10^{-3}\,\mathrm{s}^{-1}$. Likewise, the force is normalized with respect to the reference stress just mentioned and the initial cross section A of the specimen as $\tilde{F} = F/\left(A \cdot \sigma_{RD_0}\right)$.

2.3.1. Monotonic loading

At least two specimens per orientation and configuration are tested.

* Effect of the loading direction θ

Examples of quasi-static tests performed along four directions are plotted in Figure 3. According to this Figure, the highest yield stress is found along the transverse direction (which is consistent with the high fraction of c axes of the HCP phase in this direction on the pole figures in Fig.1c) followed by the rolling (along which a smaller, but non negligible fraction of c axes are aligned) and the diagonal direction, in both tension and compression. The normal direction (orthogonal to most c axes) has, accordingly, the lowest yield stress. The anisotropy is more accentuated under compression loading.

* Effect of loading sign χ=-1/3,1/3

As shown in Figure 3 for all directions and Figure 4 for the rolling direction in particular, a strong yield stress differential between tension and compression is observed. According to Figure 4, the yield stress in compression is higher than in tension by around 20 %. The hardening for both types of loading is strongly non linear at small plastic strain and tends to become linear at large plastic strain. The nonlinear part is more pronounced under compression loading while the linear part is (quasi) similar (same slope) under tension and compression loading. Similar results were found for the other directions (not shown here).

* Effect of the strain rate $\dot{\kappa}$

In Figure 5 are superimposed the results of tension and compression tests carried out at various loading rates ranging from quasi-static to dynamic regimes.

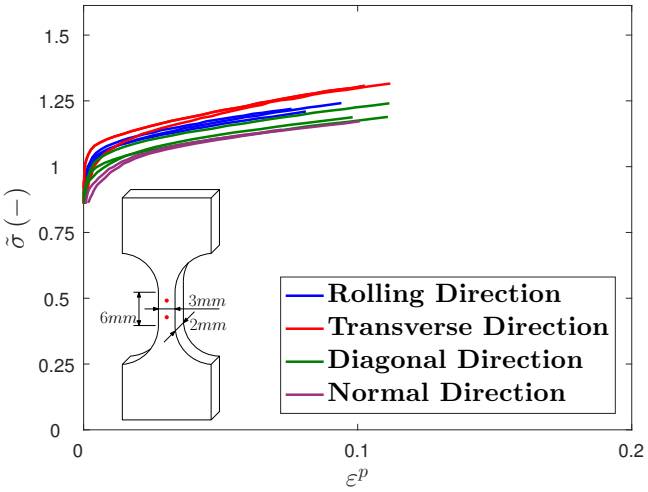

(a) Tension tests.

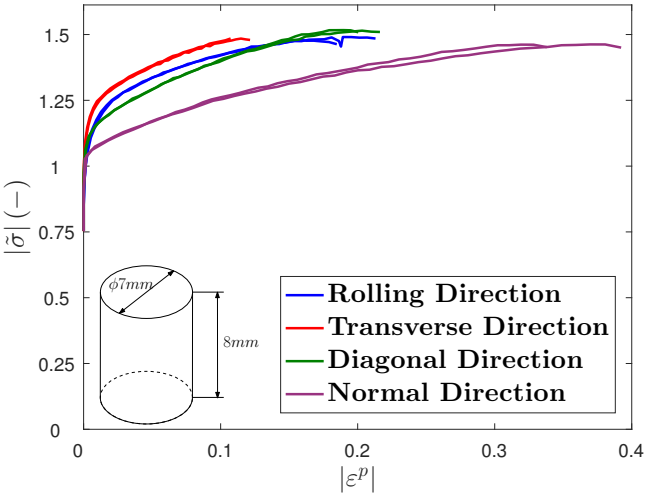

(b) Compression tests.

Figure 3: Stress vs plastic strain. Tension and compression. Influence of the direction. $|\dot{\varepsilon}| \simeq 10^{-3}\,\mathrm{s}^{-1}$, $T = 25\,^{\circ}\mathrm{C}$

.

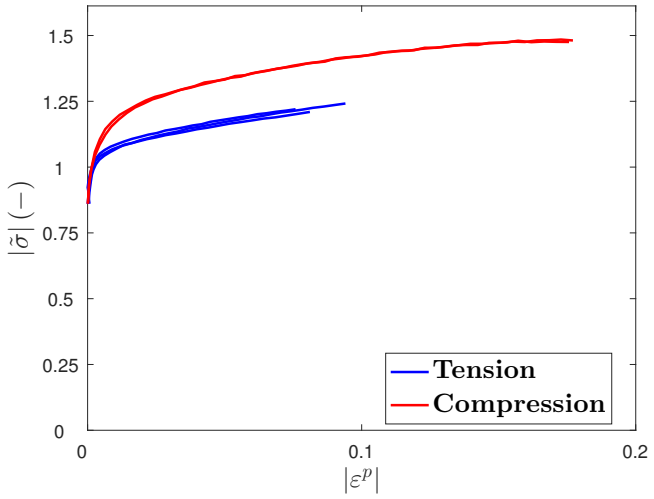

Figure 4: Stress vs plastic strain. Tension-Compression superimposition. $|\dot{\varepsilon}| \simeq 10^{-3}\,\mathrm{s}^{-1}$, $T = 25\,^{\circ}\mathrm{C}$, Rolling direction RD.

Strain rates of up to $10^{3}\,\mathrm{s}^{-1}$ were obtained. While the effect of the strain rate is not significant between $10^{-3}\,\mathrm{s}^{-1}$ and $10^{-2}\,\mathrm{s}^{-1}$, and even masked by the scatter from one specimen to the other, a clear shift can be noticed when going from the quasi-static to the dynamic range. It is noteworthy that due to inelastic self-heating at high strain rate, the specimen softens under adiabatic conditions. As a result, the hardening rate in the dynamic regime is apparently lower than in the quasi-static case. Equivalent isothermal stress-strain curves are shown later in Figure 15.

* Effect of temperature T

Figure 6 shows the results of tensile and compressive tests at various temperatures. While the yield stress decreases quasi-linearly as the temperature rises (see Figure 7), the hardening rate does not seem to be affected by the temperature under isothermal conditions.

As mentioned in the introduction, the yield stress dependence on the temperature can have a strong impact on the self-heating consequences at high loading rates. Indeed, the competition between thermal softening and plastic strain as well as strain rate hardening at high loading rates will determine the

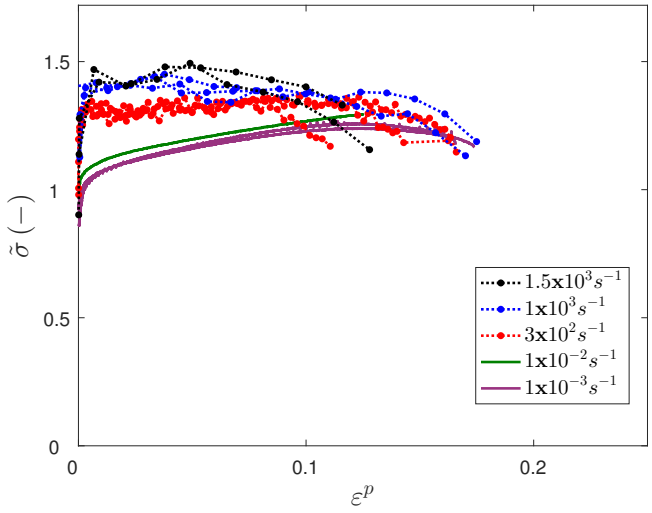

(a) Tension.

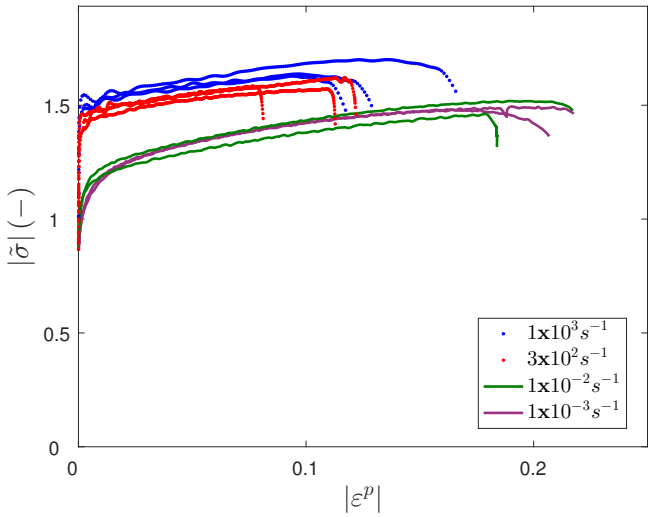

(b) Compression.

Figure 5: Stress vs plastic strain. Tension and compression. Influence of the strain rate. $T = 25\,^{\circ}\mathrm{C}$, Rolling direction RD. The dots in the high strain rate tension curves correspond to the high speed camera recording shots.

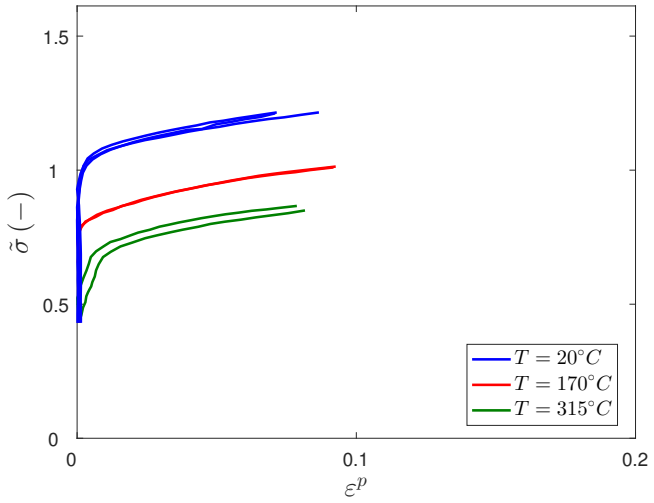

Figure 6: Stress vs plastic strain. Influence of temperature. $|\dot{\varepsilon}| \simeq 10^{-3}\,\mathrm{s}^{-1}$, Rolling direction RD. Similar effects were observed for the other directions tested as well as compression loading.

potential instability of the material.

* Effect of stress triaxiality ratio χ

Figure 8 shows the force vs. nominal strain for the specimens in Figure 2. The resistance and the ductility are highly dependent on the notch radii and resulting stress state, as expected. The highest force and lowest nominal strain at fracture is observed for the double notched specimen ($\chi \simeq 1.0$), while both single notch specimens exhibit the same peak load ($\chi \simeq 0.5 - 0.6$), but a lower fracture strain for the smaller notch radius. As for the shear specimen, a comparatively lower load and higher nominal strain at fracture is observed with respect to the other geometries.

The experimental scatter is probably due to small deviations from the nominal specimens dimension and to the macrozones present in the material (see Figure 1b).

2.3.2. Reversed loading: σ_{KH} vs σ_{IH}

In order to quantify the respective contributions of isotropic and kinematic hardening, tension-then-compression and compression-then-tension tests are car-

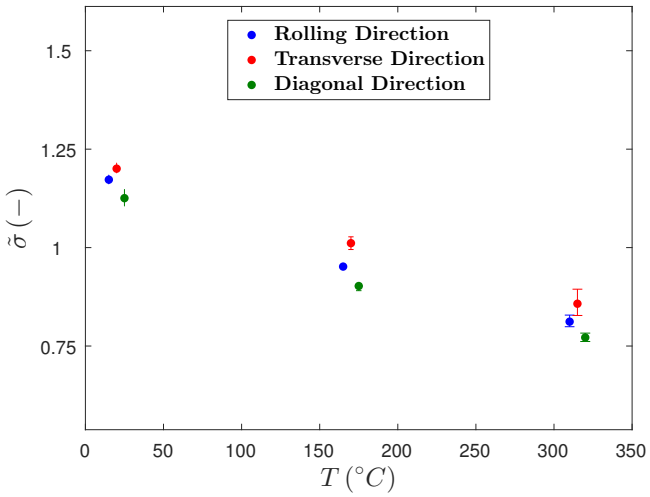

(a) Tension.

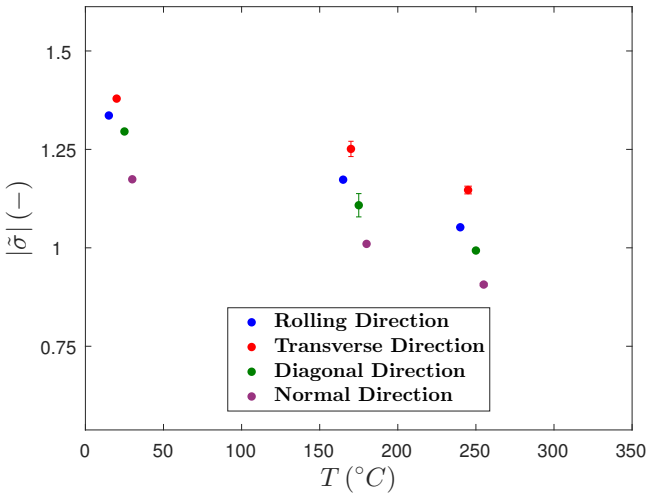

(b) Compression.

Figure 7: Stress at 5 % plastic strain vs temperature. Tension and compression. $|\dot{\varepsilon}| \simeq 10^{-3}\,\mathrm{s}^{-1}$.

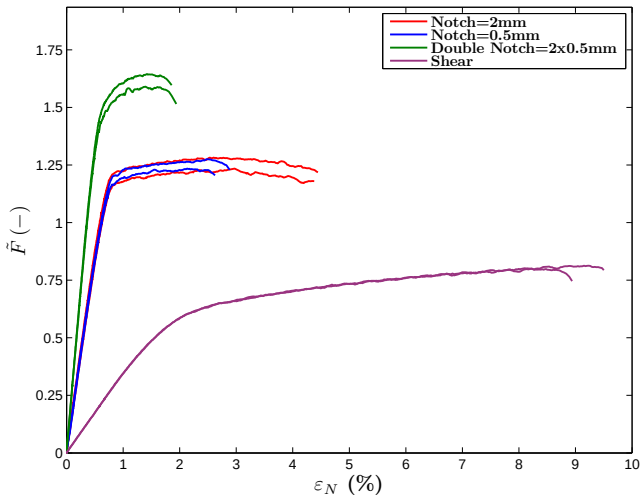

Figure 8: Load vs strain. Tension. Influence of stress triaxiality. $\dot{\varepsilon} \simeq 10^{-3}\,\mathrm{s}^{-1}$, $T = 25\,^{\circ}\mathrm{C}$, Transverse direction TD.

ried out. These two different sequences also allow to check that the strength differential deduced from separate tension and compression tests on different sample geometries is retrieved when a unique sample geometry and test setup is used.

As an example, Figure 9 shows the recorded stress-strain loops during 2.5 tension-compression cycles along the rolling direction. The isotropic and kinematic components of the material hardening can be deduced from the stress for which the stress-strain curve during unloading departs from linearity by more than a given offset [58]. For example, for an offset of $\delta\varepsilon^p = 10^{-4}$, the kinematic hardening values were found to contribute for more than 30 % to the flow stress in Ti-6Al-4V. Yet, changing the offset results in a change of the relative contributions.

2.3.3. Multi-step relaxation loading: σ_v

As deduced from tests carried out at different strain rates, a strain rate-induced overstress is present, see Figure 5 at room temperature. A series of stress relaxation periods are therefore introduced during tensile as well as com-

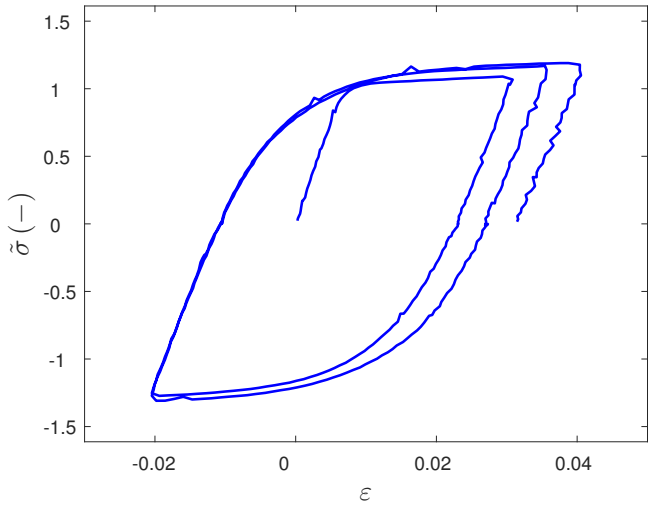

Figure 9: Stress vs strain. Alternating tension-compression test. $|\dot{\varepsilon}| \simeq 5 \times 10^{-4}\,\mathrm{s}^{-1}$, $T = 25\,^{\circ}\mathrm{C}$, Rolling direction RD.

pressive tests, in order to extract the viscous component of the flow stress. The displacement-controlled tests are interrupted at selected strain amounts and the total deformation of the specimen remains constant. A drop in stress is recorded due to viscous relaxation and the test is resumed when the stress level has reached a steady state.

In Figure 10 are plotted the stress-strain curves obtained from the multi-step relaxation loading. The dotted lines are obtained by interpolation between the end-points of the relaxation periods and represent the rate independent part of the flow stress. By subtracting it from the total stress, the viscous component can be determined from Equation 1 via

$$\sigma_v = \sigma - (\sigma_{KH} + \sigma_{IH}) \tag{2}$$

According to Figure 10, the viscous stress remains constant along the deformation in tension and compression. Furthermore, no anisotropy is found in terms of the relaxed stress. Therefore, the viscous component is considered independent of the loading direction and of the deformation. This enforces the previous simplification in Equation 1 of additive decomposition of the stress in

a strain hardening and a viscous component.

Slight differences in viscous behavior in tension and in compression can be however noticed. To check if these differences are significant or an artifact due to the differences in testing devices and specimens geometries, the cylindrical specimens used for the reversed loading are employed to measure the relaxed stress both in tension and in compression. Figure 11 shows the results of a compression-tension test with two relaxation periods in tension and compression. The viscous stress, plotted in red, does not show a significant dependence on the loading direction.

Some works have reported a temperature dependence of the strain rate sensitivity, see e.g. Tuninetti et al. [26]). For the material under consideration in the present study, this effect is weak enough to be neglected.

2.4. Analysis and discussion

By extrapolating the steady-state curves (dotted lines) in Figure 10, the rate independent initial yield stress at room temperature can be estimated for each loading direction. It can then be subtracted from the flow stress at various strain rates so as to determine the viscous stress. Similarly, the viscous stress measured in the relaxation tests can be used to obtain from Equation 1 the rate independent stress $\sigma_{KH} + \sigma_{IH} = \sigma - \sigma_v$.

In this section, the effects of anisotropy, strain hardening and temperature on the rate independent stress are analyzed as well as the viscous stress.

2.4.1. Plastic anisotropy and Strength Differential

Figure 12 shows the yield surface in the (σ_{RD},σ_{TD}) plane at various plastic strain amounts. In the case of the diagonal direction, the Cauchy stress components with respect to the rolling and transverse axes are plotted. As for the normal direction ND, the equivalent biaxial state is used. For the sake of comparison, the von Mises yield surface passing through the yield stress along the rolling direction RD is plotted to quantify the degree of anisotropy. Von Mises criterion clearly underestimates the yield stresses in compression (the compres-

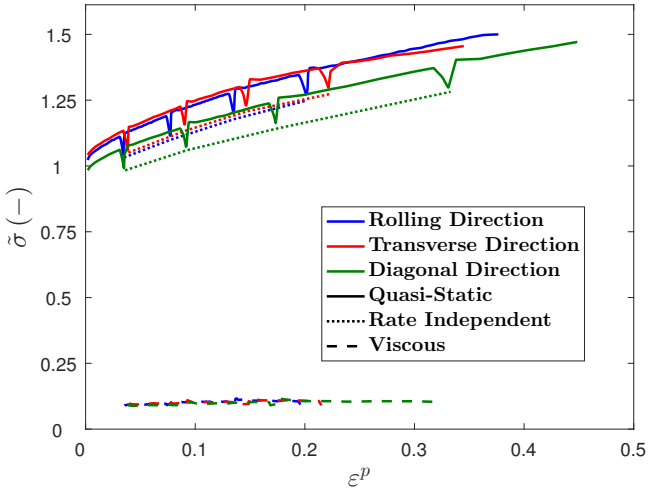

(a) Tension.

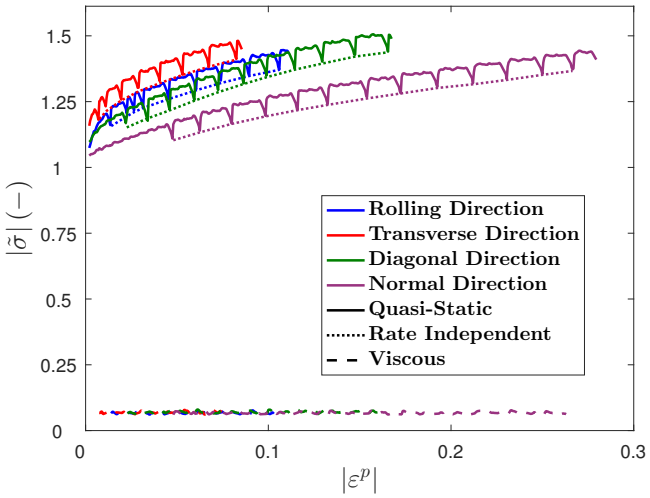

(b) Compression.

Figure 10: Stress vs plastic strain. Tension and compression. Multi-step relaxation tests. The drop in stress as the static state is achieved is defined as the strain rate induced overstress or viscous stress (plotted as a dashed line). $|\dot{\varepsilon}| \simeq 5 \times 10^{-4}\,\mathrm{s}^{-1}$, $T = 25\,^{\circ}\mathrm{C}$

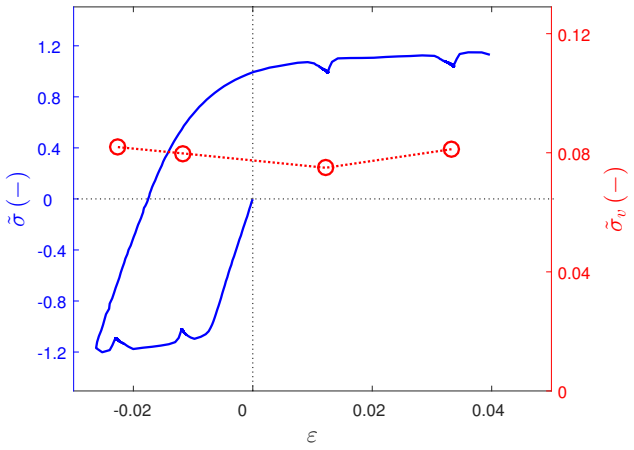

Figure 11: Stress vs strain. Compression-tension test with four relaxation periods on a cylindrical specimen. $|\dot{\varepsilon}| \simeq 5 \times 10^{-4}\,\mathrm{s}^{-1}$, $T = 25\,^{\circ}\mathrm{C}$, Rolling direction RD. The viscous stress is plotted in red.

sion under the normal direction ND is shown in the top right quadrant as a biaxial tensile state). As for the orthotropy, differences are more subtle. The yield stress in the transverse direction TD tends to be underestimated whereas those in the normal ND and diagonal DD directions are overestimated by the isotropic yield criterion. As the deformation increases, the misfit with von Mises criterion grows larger as seen in Figure 12.

2.4.2. Strain Hardening

The first cycle from Figure 9 is reconsidered here after removing the viscous component, to highlight the contributions of the isotropic and the kinematic hardening. The compressive part of the cycle has been inverted and is compared with the tension and compression monotonic stress-strain curves. As observed in Figure 13, a nonlinear kinematic hardening produces a progressive yielding during the load reversal. As the cyclic curve goes into compression, a permanent offset with respect to the monotonic compression appears, as a result of the Bauschinger effect.

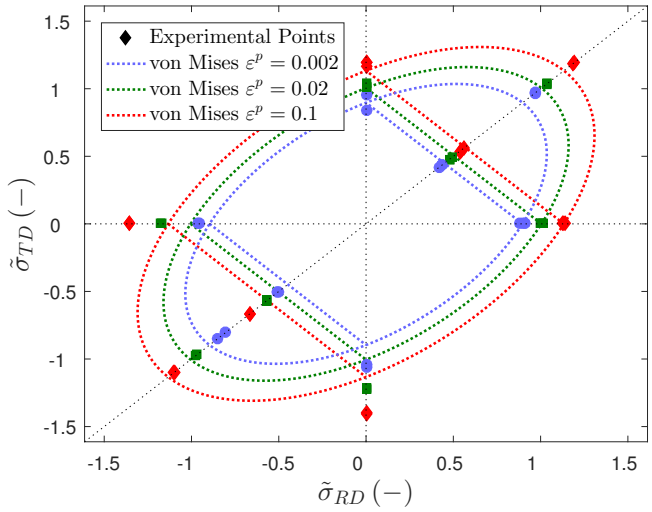

Figure 12: Yield locus in the (σ_{RD},σ_{TD}) plane, after viscous component removal. $|\dot{\varepsilon}| \simeq 10^{-3}\,\mathrm{s}^{-1}$, $T = 25\,^{\circ}\mathrm{C}$. The loading in the normal direction is considered equivalent to the biaxial stress state. The diagonal direction implicitly includes a shear component not represented in the graph.

2.4.3. Strain Rate Hardening

The viscous component from the curves in Figure 5 is plotted versus the strain rate in a logarithmic scale on Figure 14 for the tension and compression tests. The result evidences the linear evolution of the viscous component with strain rate (in the log scale). The Norton-Perzyna law is accordingly suitable to reproduce the observed results. It is expressed as

$$\sigma_v = Y_v \dot{\kappa}^{1/n_v} \tag{3}$$

2.4.4. Thermal Softening

As shown in Figure 6, the flow stress monotonically decreases with increasing temperature. Although the evolution of the flow stress with respect to temperature seems linear (see Figure 7), within the limited range of temperatures investigated, a linear extrapolation would predict negative stress values before the melting point. A power law is commonly used in literature, and it

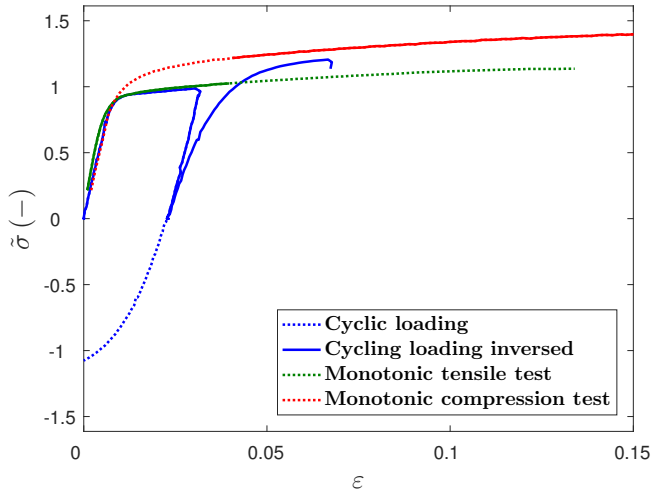

Figure 13: Stress vs strain. Strain hardening comparison between the monotonic tests and the load reversal test. $|\dot{\varepsilon}| \simeq 10^{-3}\,\mathrm{s}^{-1}$, $T = 25\,^{\circ}\mathrm{C}$ Rolling direction RD

ensures a positive stress until melting [59]:

$$\sigma \propto 1 - \langle \frac{T - T_{ref}}{T_m - T_{ref}} \rangle^{m_T} \tag{4}$$

where m_T is a material parameter, $T_m \simeq 1630\,^{\circ}\mathrm{C}$ the melting point and $T_{ref} = 25\,^{\circ}\mathrm{C}$ the reference temperature. The Macaulay brackets $\langle x \rangle = max\,(0, x)$ are used.

Under low strain rate loading the conditions are isothermal, whereas under high strain rate loading, they are (quasi) adiabatic. As a consequence, the heat generated by plastic dissipation is not evacuated fast enough by conduction, leading to a local temperature rise and the material is subject to thermal softening along the deformation process. Self-heating is usually estimated by considering that a fraction of the plastic work rate is converted into heat:

$$\Delta T \simeq \frac{\beta}{\rho c} \int_{\kappa} \sigma d\kappa \tag{5}$$

where ρ is the mass density and c is the specific heat of the material. β represents the inelastic heat fraction also called Taylor-Quinney coefficient [60]. The latter is often assumed constant with values typically ranging between 0.8

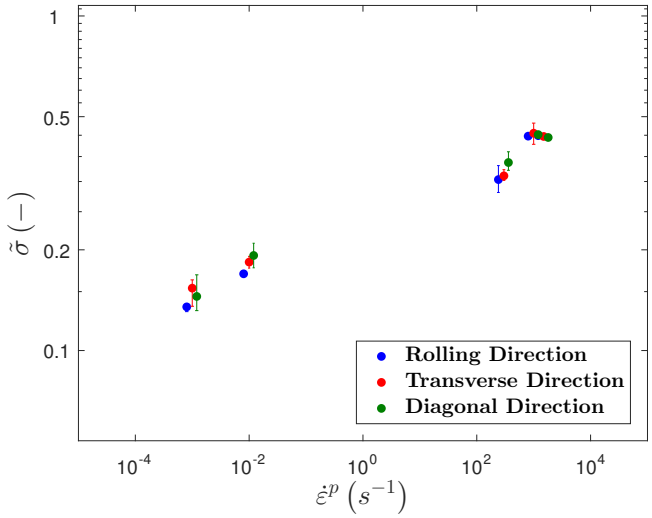

(a) Tension.

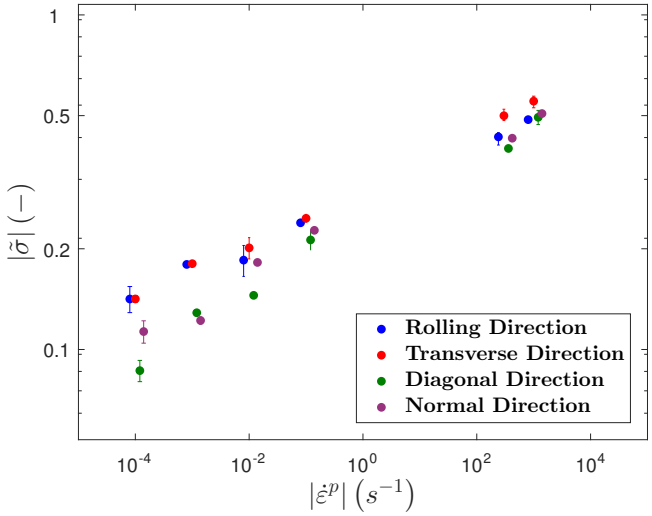

(b) Compression.

Figure 14: Stress at 2 % of plastic strain vs plastic strain rate. Tension and compression. At this plastic strain amount self-heating induced softening under high strain rate is still negligible. $T = 25\,^{\circ}\mathrm{C}$

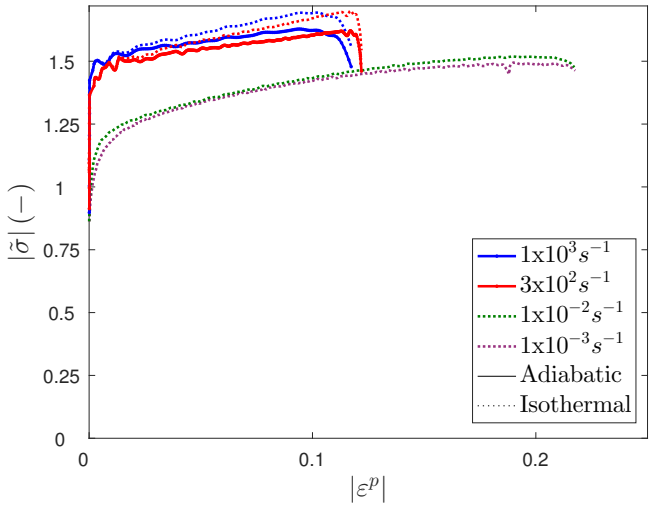

Figure 15: Stress vs plastic strain. Isothermal quasi-static and dynamic compression curves. $T = 25\,^{\circ}\text{C}$, Rolling direction RD

and 1. Experimental estimates of β for Ti-6Al-4V may be completely different from an author to another, see e.g. Mason et al. [61] and MacDougall and Harding [47], while showing that β does not keep a constant value along the deformation process. In absence of further information on the right value of β for the material under consideration, we are here assuming that $\beta = 0.9$.

Equivalent isothermal stress-strain curves may be obtained from adiabatic stress-strain curves by removing the self-heating induced thermal softening. By assuming β=0.9 and using Figure 7, isothermal dynamic compression curves can be estimated, see Figure 15. Accordingly, isothermal, quasi-static and dynamic curves exhibit a similar strain hardening.

3. Constitutive Modeling

The extensive experimental campaign detailed in the previous section has evidenced that the Ti-6Al-4V grade under consideration is subject to significant (i) anisotropic plasticity which manifests through loading direction dependence, kinematic hardening and strength differential, (ii) isotropic strain hardening, (iii) rate dependence and (iv) thermal softening. Starting from the experimental

observations, a constitutive model accounting for the above mentioned effects is built within the irreversible thermodynamics framework. More generally, the aim of the present work is to develop a constitutive model able to describe the behavior of metals and alloys within a wide range of strain, strain rate, temperature and loading path.

Kinematic considerations are first specified in the context of large elastic-plastic deformation. The general irreversible thermodynamics framework is then applied for phenomenologically describing the consequences of the underlying conservative and dissipative mechanisms. Eventually, constitutive equations are applied to the Ti-6Al-4V grade under consideration.

3.1. Finite strain framework

Moderately large elastic-plastic strains have been observed during the experimental campaign, implying a nonlinear geometric formulation. The deformation gradient $\underline{\underline{F}}$ describes the transformation from the initial (undeformed) configuration to the current (deformed) configuration of the particle coordinates of any point belonging to the material body. As suggested by [62, 63], the deformation gradient $\underline{\underline{F}}$ may be multiplicatively decomposed into an elastic contribution $\underline{\underline{F}}^e$ and a plastic contribution $\underline{\underline{F}}^p$:

$$\underline{\underline{F}} = \frac{\partial \underline{x}}{\partial \underline{X}} = \underline{\underline{F}}^e \, \underline{\underline{F}}^p \tag{6}$$

where $\underline{X}$ and $\underline{x}\,(\underline{X}, t)$ represents the particle coordinates in the initial and current configurations, respectively. In this context, $\underline{\underline{F}}^e$ represents the transformation between the virtually elastically unstressed (intermediate) configuration and current configuration, and $\underline{\underline{F}}^p$ the transformation between the initial configuration and virtually elastically unstressed (intermediate) configuration.

We are here considering an intermediate configuration virtually unstressed by a pure elastic stretching $\underline{\underline{V}}^{e\,-1}$, yielding

$$\underline{\underline{F}} = \underline{\underline{V}}^e \, \underline{\underline{Q}} \, \underline{\underline{F}}^p \tag{7}$$

where $\underline{\underline{Q}}$ represents an orthogonal transformation (rotation). The velocity gradient $\underline{\underline{l}}$ accordingly reads (see Longère et al. [64])

$$\underline{\underline{l}} = \frac{\partial \underline{v}\,(\underline{x})}{\partial \underline{x}} = \dot{\underline{\underline{F}}}\,\underline{\underline{F}}^{-1} = \overset{\nabla^e}{\underline{\underline{V}}}\,\underline{\underline{V}}^{e-1} + \underline{\underline{W}} + \underline{\underline{V}}^e\,\dot{\underline{\underline{F}}}^p\,\underline{\underline{F}}^{p-1}\underline{\underline{V}}^{e-1} \tag{8}$$

where $\underline{v}$ is the particle velocity and where $\underline{\underline{W}} = \dot{\underline{\underline{Q}}}\,\underline{\underline{Q}}^T$ represents the rate of the orthogonal transformation. The decomposition of the deformation gradient $\underline{\underline{l}}$ into a symmetric part $\underline{\underline{d}}$ and a skew-symmetric part $\underline{\underline{w}}$, viz. $\underline{\underline{l}} = \underline{\underline{d}} + \underline{\underline{w}}$, yields

$$\begin{cases} \underline{\underline{d}} = [l]^S = \underline{\underline{d}}^e + \underline{\underline{d}}^p \\ \underline{\underline{w}} = [l]^{SS} = \underline{\underline{W}} + \underline{\underline{w}}^e + \underline{\underline{w}}^p \end{cases} \tag{9}$$

where

$$\begin{cases} \underline{\underline{d}}^e = \left[\overset{\nabla^e}{\underline{\underline{V}}}\,\underline{\underline{V}}^{e-1}\right]^S \\ \underline{\underline{w}}^e = \left[\overset{\nabla^e}{\underline{\underline{V}}}\,\underline{\underline{V}}^{e-1}\right]^{SS} \end{cases}; \qquad \begin{cases} \underline{\underline{d}}^p = \left[\underline{\underline{V}}^e\,\dot{\underline{\underline{F}}}^p\,\underline{\underline{F}}^{p-1}\underline{\underline{V}}^{e-1}\right]^S \\ \underline{\underline{w}}^p = \left[\underline{\underline{V}}^e\,\dot{\underline{\underline{F}}}^p\,\underline{\underline{F}}^{p-1}\underline{\underline{V}}^{e-1}\right]^{SS} \end{cases} \tag{10}$$

yielding the following expression for the rotation rate $\underline{\underline{W}}$

$$\underline{\underline{W}} = \dot{\underline{\underline{Q}}}\,\underline{\underline{Q}}^T = \underline{\underline{w}} - \left(\underline{\underline{w}}^e + \underline{\underline{w}}^p\right) \tag{11}$$

Moreover, the objective derivative $\overset{\nabla}{\underline{\underline{a}}}$ of any second order tensor $\underline{\underline{a}}$ reads

$$\overset{\nabla}{\underline{\underline{a}}} = \dot{\underline{\underline{a}}} - \underline{\underline{W}}\,\underline{\underline{a}} + \underline{\underline{a}}\,\underline{\underline{W}} \tag{12}$$

Under small elastic strain assumption, Equation 10 reduces to

$$\begin{cases} \underline{\underline{d}}^e = \overset{\nabla^e}{\underline{\underline{V}}} \\ \underline{\underline{w}}^e = 0 \end{cases}; \begin{cases} \underline{\underline{d}}^p = \left[\dot{\underline{\underline{F}}}^p\,\underline{\underline{F}}^{p-1}\right]^S \\ \underline{\underline{w}}^p = \left[\dot{\underline{\underline{F}}}^p\,\underline{\underline{F}}^{p-1}\right]^{SS} \end{cases} \tag{13}$$

In addition, assuming tentatively negligible effect of the spin $\underline{\underline{w}}^p$ in regards with the spin $\underline{\underline{w}}$ (see the assumption of moderate plastic strain in Schieck and Stumpf [65]), Equation 11 reduces to

$$\underline{\underline{W}} = \underline{\underline{w}} \tag{14}$$

where the assumption of negligible effects of anisotropy is also used [66].

According to the decomposition of the deformation gradient $\underline{\underline{F}}$ in Equation 7, when working with respect to the current configuration, it is needed to use the Zaremba-Jaumann objective derivative. Alternatively, it is possible to work with respect to the $\underline{\underline{Q}}$-rotated or co-rotational configuration, by means of a push forward and a pull back rotations [67, 68]. The latter method is used in the following. The rate equations of the constitutive model are consequently formulated by using time derivatives with respect to the co-rotational frame:

$$\dot{\underline{\underline{a}}}_Q = \underline{\underline{Q}}^T \overset{\nabla}{\underline{\underline{a}}} \underline{\underline{Q}} \tag{15}$$

For example the Cauchy stress would read in the context of temperature independent hypo-elasticity as

$$\overset{\nabla}{\underline{\underline{\sigma}}} = \underline{\underline{\underline{\underline{C}}}} : \underline{\underline{d}}^e \quad \rightarrow \quad \dot{\underline{\underline{\sigma}}}_Q = \underline{\underline{\underline{\underline{C}}}} : \dot{\underline{\underline{\varepsilon}}}^e_Q \tag{16}$$

In the sequel, the subscript $\cdot_Q$ is dropped for simplicity.

3.2. Irreversible thermodynamics framework

Constitutive state laws and complementary laws respectively derived from the state and dissipation potentials are expressed in this subsection.

3.2.1. State potential and constitutive state laws

The internal variable procedure is herein applied within the irreversible thermodynamics framework to model the thermo-mechanical behavior of the Ti-6Al-4V grade under consideration. The instantaneous state of the material is assumed to be well described via the Helmholtz free energy Ψ whose arguments are the absolute temperature T, the elastic strain tensor $\underline{\underline{\varepsilon}}^e$, the isotropic hardening variable (also called cumulated plastic strain) κ, and the kinematic hardening variable $\underline{\underline{\alpha}}$. Therefore, the Helmholtz state potential can be decomposed into four parts: a recoverable energy Ψ_e, a purely thermal part Ψ_T and two stored energies corresponding to the isotropic and kinematic hardening contributions, Ψ_{pI} and Ψ_{pK}, see [69]. Considering tentatively state uncoupling between the

two mechanisms of plasticity and between them and elasticity, the Helmholtz free energy Ψ is taken of the form

$$\Psi\left(\underline{\underline{\varepsilon}}^e, \kappa, \underline{\underline{\alpha}}; T\right) = \Psi_e\left(\underline{\underline{\varepsilon}}^e; T\right) + \Psi_T\left(T\right) + \Psi_{pI}\left(\kappa; T\right) + \Psi_{pK}\left(\underline{\underline{\alpha}}\right) \tag{17}$$

where Ψ_{pK} is taken as temperature independent. The specific contributions to the state potential are defined as

$$\begin{cases} \rho\Psi_e\left(\underline{\underline{\varepsilon}}^e; T\right) = \dfrac{1}{2}\underline{\underline{\varepsilon}}^e : \underline{\underline{\underline{\underline{C}}}} : \underline{\underline{\varepsilon}}^e - \alpha K\left(T - T_0\right) trace(\underline{\underline{\varepsilon}}^e) \\ \rho\Psi_T = -\dfrac{\rho c}{2T_0}\Delta T^2 \\ \rho\Psi_{pI}\left(\kappa; T\right) = h\left(\kappa\right) g\left(T\right) \\ \rho\Psi_{pK}\left(\underline{\underline{\alpha}}\right) = \dfrac{1}{3} C \underline{\underline{\alpha}} : \underline{\underline{\alpha}} \end{cases} \tag{18}$$

where ρ is the mass density, $\underline{\underline{\underline{\underline{C}}}}$ is the elasticity stiffness fourth order tensor, with $C_{ijkl} = \lambda\delta_{ij}\delta_{kl} + \mu\left(\delta_{ik}\delta_{jl} + \delta_{il}\delta_{jk}\right)$, λ and μ being the Lamé coefficients, K the bulk modulus, with $K = \lambda + \frac{2}{3}\mu$, α the thermal dilatation coefficient, T_0 the initial temperature, and c is the specific heat. $h\left(\kappa\right)$ and $g\left(T\right)$ are the stored energy of cold work and the thermal softening function, respectively, and the scalar C is a kinematic hardening-related parameter.

The thermodynamic forces derived from the state potential with respect to their conjugate variables are given by the constitutive state laws defined below.

$$\begin{cases} \underline{\underline{\sigma}} = \rho\left.\dfrac{\partial\Psi}{\partial\underline{\underline{\varepsilon}}^e}\right|_{\kappa,\underline{\underline{\alpha}},T} = \rho\left.\dfrac{\partial\Psi_e}{\partial\underline{\underline{\varepsilon}}^e}\right|_{T} = \underline{\underline{\underline{\underline{C}}}} : \underline{\underline{\varepsilon}}^e - \alpha K\left(T - T_0\right)\underline{\underline{I}} \\ \rho s = -\rho\left.\dfrac{\partial\Psi}{\partial T}\right|_{\underline{\underline{\varepsilon}}^e,\kappa,\underline{\underline{\alpha}}} = -\rho\left(\left.\dfrac{\partial\Psi_e}{\partial T}\right|_{\underline{\underline{\varepsilon}}^e} + \dfrac{\partial\Psi_T}{\partial T} + \left.\dfrac{\partial\Psi_{pI}}{\partial T}\right|_{\kappa}\right) \\ \qquad\qquad = \alpha K trace\left(\underline{\underline{\varepsilon}}^e\right) + \dfrac{\rho c}{T_0}\Delta T - h\left(\kappa\right) g'\left(T\right) \\ r = \rho\left.\dfrac{\partial\Psi}{\partial\kappa}\right|_{\underline{\underline{\varepsilon}}^e,\underline{\underline{\alpha}},T} = \rho\left.\dfrac{\partial\Psi_{pI}}{\partial\kappa}\right|_{T} = h'\left(\kappa\right) g\left(T\right) \\ \underline{\underline{X}} = \rho\left.\dfrac{\partial\Psi}{\partial\underline{\underline{\alpha}}}\right|_{\underline{\underline{\varepsilon}}^e,\kappa,T} = \rho\left.\dfrac{\partial\Psi_{pK}}{\partial\underline{\underline{\alpha}}}\right|_{T} = \dfrac{2}{3} C \underline{\underline{\alpha}} \end{cases} \tag{19}$$

where $\underline{\underline{\sigma}}$ is the Cauchy stress tensor, s the entropy, r the isotropic hardening force and $\underline{\underline{X}}$ the kinematic hardening force.

Finally, the Gibbs relation reads

$$\rho\dot{\Psi} = \underline{\underline{\sigma}} : \dot{\underline{\underline{\varepsilon}}}^e + r\dot{\kappa} + \underline{\underline{X}} : \dot{\underline{\underline{\alpha}}} - \rho s\dot{T} \tag{20}$$

3.2.2. Dissipation and complementary laws

Injecting the Gibbs relation into Clausius-Duhem inequality and using $\dot{\underline{\underline{\varepsilon}}} = \dot{\underline{\underline{\varepsilon}}}^e + \dot{\underline{\underline{\varepsilon}}}^p$ yield the following expression for the intrinsic dissipation

$$\begin{aligned} \mathcal{D} &= \underline{\underline{\sigma}} : \dot{\underline{\underline{\varepsilon}}} - \rho\left(\dot{\Psi} + s\dot{T}\right) \\ &= \underline{\underline{\sigma}} : \dot{\underline{\underline{\varepsilon}}}^p - r\dot{\kappa} - \underline{\underline{X}} : \dot{\underline{\underline{\alpha}}} \quad \geq 0 \end{aligned} \tag{21}$$

which involves force-related quantities $A = \left(\underline{\underline{\sigma}}, r, \underline{\underline{X}}\right)$ and flux-related quantities $\dot{a} = \left(\dot{\underline{\underline{\varepsilon}}}^p, -\dot{\kappa}, -\dot{\underline{\underline{\alpha}}}\right)$. In the context of the normality rule, the dissipation may be rewritten in the following form

$$\mathcal{D} = A\dot{a} = A\dot{\lambda}\frac{\partial F}{\partial A} \geq 0 \tag{22}$$

where F is the plastic potential meeting the required conditions of positiveness and convexity and where $\dot{\lambda}$ is the positive plastic multiplier. In the context of rate dependent non-associated plasticity, $\dot{\lambda}$ is assumed to derive from a dissipation potential $\Omega(f)$, viz. $\dot{\lambda} = \partial\Omega/\partial f$, where f represents the yield function.

The yield function f and plastic potential F are written of the form

$$\begin{aligned} f\left(\underline{\underline{\sigma}}, r, \underline{\underline{X}}, ...\right) &= \sigma_{eq}\left(\underline{\underline{\sigma}}, \underline{\underline{X}}, ...\right) - \sigma_y\left(r, ...\right) = \sigma_v\left(\dot{\kappa}, ...\right) \geq 0 \\ F\left(\underline{\underline{\sigma}}, r, \underline{\underline{X}}, ...\right) &= f + \hat{f}\left(\underline{\underline{X}}\right) \end{aligned} \tag{23}$$

where σ_{eq} is the transformed equivalent stress accounting for the different sources of plastic anisotropy, σ_y the rate independent yield stress, σ_v the strain rate induced overstress or viscous stress, and where ... represents other arguments defined later. $\hat{f}\left(\underline{\underline{X}}\right)$ is a function involving non-linearity in kinematic hardening.

The normality rule accordingly yields

$$\begin{cases} \underline{\underline{\dot{\varepsilon}}}^p = \dot{\lambda}\dfrac{\partial F}{\partial \underline{\underline{\sigma}}} = \dot{\lambda}\dfrac{\partial \sigma_{eq}}{\partial \underline{\underline{\sigma}}} = \dot{\lambda}\underline{\underline{n}} \quad \text{with} \quad \underline{\underline{n}} = \dfrac{\partial \sigma_{eq}}{\partial \underline{\underline{\sigma}}} \\ \dot{\kappa} = -\dot{\lambda}\dfrac{\partial F}{\partial r} = -\dot{\lambda}\dfrac{\partial f}{\partial r} = \dot{\lambda} \\ \underline{\underline{\dot{\alpha}}} = -\dot{\lambda}\dfrac{\partial F}{\partial \underline{\underline{X}}} = -\dot{\lambda}\left(\dfrac{\partial f}{\partial \underline{\underline{X}}} + \dfrac{\partial \hat{f}}{\partial \underline{\underline{X}}}\right) = \dot{\lambda}\underline{\underline{m}} \quad \text{with} \quad \underline{\underline{m}} = -\left(\dfrac{\partial \sigma_{eq}}{\partial \underline{\underline{X}}} + \dfrac{\partial \hat{f}}{\partial \underline{\underline{X}}}\right) \end{cases} \tag{24}$$

These laws are completed by the temperature rise coming from adiabatic self-heating under high strain rate loading assuming negligible contributions of thermo-elastic and thermo-plastic couplings [70]. Temperature rise is estimated from dissipation in Equation 21, see Longère and Dragon [71], according to

$$\rho c \dot{T} \simeq \mathcal{D} = \underline{\underline{\sigma}} : \underline{\underline{\dot{\varepsilon}}}^p - r\dot{\kappa} - \underline{\underline{X}} : \underline{\underline{\dot{\alpha}}} \geq 0 \tag{25}$$

3.3. Constitutive equations

Quantities introduced in the previous subsection are now specified for the material under consideration in agreement with the experimental observations.

3.3.1. Transformed equivalent stress σ_{eq}

Plastic anisotropy entails a loss of coaxiality between the plastic strain rate and the stress deviator. As the plastic strain rate is derived from the transformed equivalent stress according to the normality rule, the plastic anisotropy effects are accounted for in the expression of the transformed equivalent stress. It is reminded that in the present case plastic anisotropy manifests through (i) loading direction dependence, (ii) kinematic hardening, and (iii) strength differential.

We are here considering the transformed equivalent stress σ_{eq} as a function of three variables, namely the current Cauchy stress second order tensor $\underline{\underline{\sigma}}$, the back stress second order tensor $\underline{\underline{X}}$, and a fourth order tensor accounting for the

texture-induced orthotropy $\underline{\underline{\underline{\underline{A}}}}$.

$$\sigma_{eq} = \sigma_{eq}\left(\underline{\underline{\sigma}}, \underline{\underline{X}}; \underline{\underline{\underline{\underline{A}}}}\right) \tag{26}$$

Each source of anisotropy is first studied independently of the others and then a combination of the three sources is proposed.

* Texture-induced initial orthotropy: $\underline{\underline{X}} = \underline{\underline{0}}$

Following Karafillis and Boyce [12], we introduce the transformed stress $\underline{\underline{\Sigma}} = \underline{\underline{\underline{\underline{A}}}} : \underline{\underline{\sigma}}$ also denoted as the Isotropy Plasticity Equivalent (IPE) stress. The fourth order tensor $\underline{\underline{\underline{\underline{A}}}}$ is a linear multiplicative operator involving potential plastic orthotropy. In the case of an isotropic material, the operator reduces to the identity tensor, viz. $\underline{\underline{\underline{\underline{A}}}} = \underline{\underline{\underline{\underline{I}}}}$. As a consequence, the transformed stress reads

$$\sigma_{eq}\left(\underline{\underline{\sigma}}, \underline{\underline{X}}; \underline{\underline{\underline{\underline{A}}}}\right) = \sigma_{eq}\left(\underline{\underline{\Sigma}}, \underline{\underline{X}}\right) \tag{27}$$

Table 1 reports two definitions of the transformed equivalent stress aiming at accounting for anisotropic plasticity: (i) by incorporating the tensor $\underline{\underline{\underline{\underline{A}}}}$ directly in the expression of the equivalent stress, as proposed by Hill [6], and (ii) by incorporating it at the stress level, as proposed by Karafillis and Boyce [12].

Table 1: Definitions of transformed equivalent stress in the case of orthotropic plasticity.

Hill (1948)	**K&B (1993)**
$\sigma_{eq}^2 = \frac{1}{2}\underline{\underline{\sigma}} : \underline{\underline{\underline{\underline{A}}}} : \underline{\underline{\sigma}}$	$\underline{\underline{\Sigma}} = \underline{\underline{\underline{\underline{A}}}} : \underline{\underline{\sigma}}$ $\sigma_{eq}^2 = \frac{1}{2}\underline{\underline{\Sigma}} : \underline{\underline{\Sigma}}$

The fourth order tensor accounting for anisotropic plasticity can be simplified as a 6x6 matrix according to major and minor symmetries while stress second

order tensors are reduced to vectors according to Voigt or Bechterew notations.

$$\underline{\underline{\underline{\underline{A}}}} = \begin{bmatrix} A_{11} & A_{12} & A_{13} & & & \\ A_{12} & A_{22} & A_{23} & & & \\ A_{13} & A_{23} & A_{33} & & & \\ & & & A_{44} & & \\ & & & & A_{55} & \\ & & & & & A_{66} \end{bmatrix} \tag{28}$$

In case of pressure independent-orthotropic plasticity, following condition in Equation 29 for anisotropy coefficients in Equation 28 is required and Hill48 [6] orthotropic matrix is retrieved with 6 independent anisotropy coefficients.

$$\begin{cases} A_{11} = -\left(A_{12} + A_{13}\right) \\ A_{22} = -\left(A_{12} + A_{23}\right) \\ A_{33} = -\left(A_{13} + A_{23}\right) \end{cases} \tag{29}$$

We are here adopting the 9-anisotropy-coefficient approach in Equation 28 and the pressure independence will be described by applying the linear transformation $\underline{\underline{\underline{\underline{A}}}}$ to the stress deviator tensor and not to the stress tensor itself, see Equation 32 and Table 2 later on.

* Kinematic hardening-induced evolving anisotropy $\underline{\underline{\underline{\underline{A}}}} = \underline{\underline{\underline{\underline{I}}}}$

The approach commonly adopted when dealing with kinematic plastic hardening is to consider the translation of the yield surface by means of the deviatoric back stress $\underline{\underline{X}}$. For instance, the transformed equivalent stress would read

$$\sigma_{eq}^2 = \frac{3}{2}\left(\underline{\underline{s}} - \underline{\underline{X}}\right) : \left(\underline{\underline{s}} - \underline{\underline{X}}\right) = \frac{3}{2}\underline{\underline{\hat{s}}} : \underline{\underline{\hat{s}}} \tag{30}$$

where $\underline{\underline{\hat{s}}} = \left(\underline{\underline{s}} - \underline{\underline{X}}\right)$

* Strength differential-induced initial anisotropy $\underline{\underline{\underline{\underline{A}}}} = \underline{\underline{\underline{\underline{I}}}}$ & $\underline{\underline{X}} = \underline{\underline{0}}$

The strength differential between tension and compression can be assumed to be a type of anisotropy. As mentioned in the introduction, CPB06 [25], Khan [24] and Longère [31] propose different methods for describing this effect.

In this study, the CPB06 model [25] is chosen as it allows for a simple definition of the yield surface without resorting to the Lode angle or a coupling with the viscous component. The CPB06 isotropic yield surface adds a strength differential parameter k to the definition in Karafillis and Boyce [12] resulting in the form

$$\sigma_{eq}{}^{a} = \frac{1}{m_0{}^{a}} \left\{ (|S_1| - kS_1)^a + (|S_2| - kS_2)^a + (|S_3| - kS_3)^a \right\} \tag{31}$$

where S_p are the eigenvalues of the stress tensor $\underline{\underline{\sigma}}$, k is the main parameter defining the material asymmetry, a is a shape parameter of the yield surface, see Hosford [72] and m_0 is a model constant.

The Karafillis and Boyce [12] generalized yield criterion can be recovered for $k = 0$ (and the Mises criterion with $a = 2$). The CPB06 criterion in Equation 31 can thus be considered as an extended distortion (without a rotation) of such surface.

* Complete transformed equivalent stress $\underline{\underline{\underline{\underline{A}}}} \neq \underline{\underline{\underline{\underline{I}}}}$ & $\underline{\underline{X}} \neq \underline{\underline{0}}$

In order to couple kinematic hardening and plastic orthotropy, two approaches can be considered, see Table 2. Following Baltov and Sawczuk [10], the back stress is first subtracted from the deviatoric stress tensor and the Hill criterion is then applied. Alternatively, Karafillis and Boyce [12] make use of their linear operator to transform the difference between the stress tensor and the back force.

On the other hand, coupling plastic orthotropy and strength differential may be achieved following CPB06 [25] approach. Indeed, the authors apply a linear transformation to the stress deviator: Σ_p is defined as the eigenvalues of the transformed tensor $\underline{\underline{\Sigma}} = \underline{\underline{\underline{\underline{A}}}} : \underline{\underline{s}}$ which replaces $\underline{\underline{s}}$ in Equation 31, see Table 2. The authors initially proposed a symmetric definition of the 6x6 matrix representation of the tensor $\underline{\underline{\underline{\underline{A}}}}$ as in Equation 28, although further simplifications using a Hill-like matrix can be made to model the orthotropy as found in [73].

We are here coupling kinematic hardening, plastic orthotropy and strength differential by combining Karafillis and Boyce [12] and CPB06 [25] methods.

For that purpose, we are defining the transformed stress eigenvalues as follows, see Table 2.

$$\begin{aligned} \hat{\Sigma}_p &= eig(\hat{\underline{\underline{\Sigma}}}); \\ \hat{\underline{\underline{\Sigma}}} &= \underline{\underline{\underline{\underline{A}}}} : \left(\underline{\underline{s}} - \underline{\underline{X}}\right) \end{aligned} \tag{32}$$

Therefore, the complete anisotropic criterion reads

$$\sigma_{eq}{}^a = \frac{1}{{m_0}^a} \left\{ \left(|\hat{\Sigma}_1| - k\hat{\Sigma}_1 \right)^a + \left(|\hat{\Sigma}_2| - k\hat{\Sigma}_2 \right)^a + \left(|\hat{\Sigma}_3| - k\hat{\Sigma}_3 \right)^a \right\} \tag{33}$$

The constant m_0 is defined such that the equivalent stress is equal to the uniaxial stress in tension (compression) if $k > 0$ ($k < 0$) for an isotropic material, i.e. $\underline{\underline{\underline{\underline{A}}}} = \underline{\underline{\underline{\underline{I}}}}$.

$${m_0}^a = \left[\frac{2}{3} \left(1 - |k| \right) \right]^a + 2 \left[\frac{1}{3} \left(1 + |k| \right) \right]^a \tag{34}$$

The coefficients A_{55} and A_{66} are herein assumed to be 1 due to the lack of information for shear along the normal direction (an alternative approach is to consider $A_{44} = A_{55} = A_{66}$ as done by Tuninetti and Habraken [26]).

Table 2: Examples of anisotropic plasticity-oriented transformed equivalent stress.

B&S (1965)	**K&B (1993)**	**CPB06**	**Present approach**
$\hat{\underline{\underline{s}}} = \underline{\underline{s}} - \underline{\underline{X}}$ $\sigma_{eq}^2 = \frac{1}{2} \hat{\underline{\underline{s}}} : \underline{\underline{\underline{\underline{A}}}} : \hat{\underline{\underline{s}}}$	$\hat{\underline{\underline{\Sigma}}} = \underline{\underline{\underline{\underline{A}}}} \left(\underline{\underline{\sigma}} - \underline{\underline{X}} \right)$ $\sigma_{eq}^2 = \frac{1}{2} \hat{\underline{\underline{\Sigma}}} : \hat{\underline{\underline{\Sigma}}}$	$\Sigma_p = eig(\underline{\underline{\Sigma}})$ $\underline{\underline{\Sigma}} = \underline{\underline{\underline{\underline{A}}}} : \underline{\underline{s}}$ $\sigma_{eq} = \sigma_{eq} \left(\Sigma_p, k \right)$	$\hat{\Sigma}_p = eig(\hat{\underline{\underline{\Sigma}}})$ $\hat{\underline{\underline{\Sigma}}} = \underline{\underline{\underline{\underline{A}}}} : \left(\underline{\underline{s}} - \underline{\underline{X}} \right)$ $\sigma_{eq} = \sigma_{eq} \left(\hat{\Sigma}_p, k \right)$

3.3.2. Viscous stress σ_v

Regarding the rate dependent formulation, the experimental results show the existence of a strain rate induced overstress independent of the anisotropy axes and plastic strain and whose temperature dependence within the temperature

range of interest is negligible. The Norton-Perzyna law is proposed to describe such behavior [74].

$$\sigma_v = Y_v \dot{\kappa}^{1/n_v} \tag{35}$$

where Y_v and n_v are material coefficients.

By following the approach in Perzyna [75], the potential described in Equation 22 is accordingly of the form

$$\Omega(f) = \frac{1}{n_v + 1} \langle \frac{f}{Y_v} \rangle^{n_v+1} \tag{36}$$

Indeed, by combining 24.2 and 36, the Norton-Perzyna law in Equation 35 is retrieved

$$\dot{\kappa} = \dot{\lambda} = \frac{\partial \Omega}{\partial f} = \langle \frac{f}{Y_v} \rangle^n = \langle \frac{\sigma_v}{Y_v} \rangle^n \tag{37}$$

3.3.3. Rate independent yield stress σ_y

The radius of the elasticity domain is defined as a temperature dependent initial threshold stress $\sigma_{y0}(T)$ plus the stress related to the isotropic hardening $\mathrm{r}(\kappa, T)$. Both the initial threshold stress and isotropic hardening force are assumed to depend on temperature according to the same thermal softening function $g(T)$:

$$\sigma_y = \sigma_{y0}(T) + r(\kappa, T) = g(T) R(\kappa) \tag{38}$$

* Strain hardening

For the definition of the isotropic hardening, the Swift (power) law and the Voce (exponential with saturation) law are widely used (see [54, 76] for a linear combination of both). For the material under consideration, some initial constant calibration (not shown here) from the monotonic tests have shown that Swift law fits well the experimental curves. On the other hand, Chun et al. [38] and Carbonnière [39] have shown that a coupling between

isotropic and kinematic hardening is well described by adding a negative Voce-type exponential law in the expression of the strain hardening function.

Therefore, a combination of Swift and (negative) Voce expressions is herein considered in view of coupling isotropic and kinematic hardening. The adopted forms for the strain hardening function $h'(\kappa)$ in Equation 19 and radius $R(\kappa)$ in Equation 38 read

$$\begin{aligned} h'(\kappa) &= Q_0(\varepsilon_0+\kappa)^n - \frac{C}{D}(1-exp(-D\kappa)) \\ R(\kappa) &= R_0 + h'(\kappa) \end{aligned} \tag{39}$$

where R_0, Q_0, ε_0 and n are the Swift law-related postive constants and C and D are (negative) Voce law-related positive constants.

* Thermal softening

As previously evidenced by the experimental campaign, the thermal softening function g(T) is of the form

$$g(T) = 1 - \langle \frac{T-T_{ref}}{T_m - T_{ref}} \rangle^{m_T} \tag{40}$$

where T_m is the melting point and T_{ref} and m_T material constants.

3.3.4. Complementary laws

Following the decomposition made in Equation 24, the plastic strain rate is expressed as

$$\underline{\underline{\dot{\varepsilon}}}^p = \dot{\kappa}\frac{\partial \sigma_{eq}}{\partial \underline{\underline{\sigma}}} = \dot{\kappa}\underline{\underline{n}} \tag{41}$$

where $\underline{\underline{n}} = \partial\sigma_{eq}/\partial\underline{\underline{\sigma}}$ represents the yield direction. It can be shown that the explicit expression for $\underline{\underline{n}}$ is

$$\underline{\underline{n}} = \sum_{p=1}^{3}\left[\frac{1}{m_0^a}\left(\frac{|\hat{\Sigma}_p| - k\hat{\Sigma}_p}{\sigma_{eq}}\right)^{a-1}\left(sgn\left(\hat{\Sigma}_p\right)-k\right)\right]\underline{\underline{\underline{J}}} : \underline{\underline{\underline{A}}} : \left(\underline{v}_p \otimes \underline{v}_p\right) \tag{42}$$

where $\underline{v}_p$ is the eigenvector corresponding to the eigenvalue $\hat{\Sigma}_p$. The outer product $\cdot \otimes \cdot$ is here used and $\underline{\underline{\underline{\underline{J}}}}$ is the fourth order tensor projecting $\underline{\underline{\sigma}}$ onto its deviatoric plane $\underline{\underline{s}}$. The deviator operator $\underline{\underline{\underline{\underline{J}}}}$ is defined in the index form as

$$J_{ijkl} = \left[\frac{1}{2}\left(\delta_{ik}\delta_{jl} + \delta_{il}\delta_{jk}\right) - \frac{1}{3}\delta_{ij}\delta_{kl}\right] \tag{43}$$

To describe nonlinear kinematic hardening, function $\hat{f}\left(\underline{\underline{X}}\right)$ in Eq 23 is taken of the form (see [35])

$$\hat{f}\left(\underline{\underline{X}}\right) = \frac{3D}{4C}\underline{\underline{X}} : \underline{\underline{X}} \tag{44}$$

The rate of the kinematic hardening variable in Equation 24 accordingly reads

$$\dot{\underline{\underline{\alpha}}} = -\dot{\kappa}\left(\frac{\partial f}{\partial \underline{\underline{X}}} + \frac{3D}{2C}\underline{\underline{X}}\right) = \dot{\kappa}\underline{\underline{m}} \tag{45}$$

It can be easily shown that $\partial\sigma_{eq}/\partial\underline{\underline{X}} = -\underline{\underline{n}}$. With this expression, the normal tensor $\underline{\underline{m}}$ recovers the non linear definition seen in Armstrong and Frederick [36] and Chaboche [37]:

$$\begin{aligned} \underline{\underline{m}} &= \underline{\underline{n}} - \frac{3D}{2C}\underline{\underline{X}} \\ \dot{\underline{\underline{\alpha}}} &= \dot{\underline{\underline{\varepsilon}}}^p - D\dot{\kappa}\underline{\underline{\alpha}} \end{aligned} \tag{46}$$

It is noteworthy that the material constants C and D coincide with the Voce law constants in Equation 39.

Injecting the different expressions in Equations 41 and 46 into Equation 25 yields the following expression for the temperature rise

$$\dot{T} = \frac{1}{\rho c}\left(\sigma_{eq} - r + \frac{2}{3}CD\underline{\underline{\alpha}} : \underline{\underline{\alpha}}\right)\dot{\kappa} \tag{47}$$

As mentioned previously, the temperature rise is usually estimated via the inelastic heat fraction β, also known as the Taylor-Quinney coefficient [60],

defined as the fraction of the plastic work rate converted into heat, or

$$\dot{T} = \frac{\beta}{\rho c}\sigma_{vm}\dot{\kappa} \tag{48}$$

The coefficient β is often arbitrarily assumed constant with a value typically ranging from 0.8 to 1.0 without much physical motivation to back it up [77] and despite many experimental evidences of its dependence on strain and even strain rate and temperature itself (see Macdougall and Harding [47]). As done in Longère [59], this coefficient may be deduced consistently from the constitutive model. In the present case, it reads

$$\beta = \frac{\sigma_{eq} - r + \frac{2}{3}CD\underline{\underline{\alpha}} : \underline{\underline{\alpha}}}{\sigma_{vm}} \tag{49}$$

This expression for β intrinsically accounts for potential dependence on strain, strain rate and temperature and is used in the sequel. In the present work, following a thermodynamic approach, the inelastic heat fraction β is consistently deduced from the constitutive model and accordingly evolves along the loading path. For high strain rate tension loading, starting from a value close to 0.95, β is slightly decreasing with increasing strain, reaching a value close to 0.8 at 0.3 of plastic strain. This evolution for β is close to the one reported in Rosakis et al. [78].

3.4. Summary of the constitutive equations

Rate equations of the constitutive model are summarized below.

* Constitutive state laws

$$\begin{cases} \dot{\underline{\underline{\sigma}}} = \underline{\underline{\underline{\underline{C}}}} : \dot{\underline{\underline{\varepsilon}}}^e - \alpha K \dot{T} \\ \dot{\underline{\underline{X}}} = \dfrac{2}{3} C \dot{\underline{\underline{\alpha}}} \\ \dot{r} = h''(\kappa)\, g(T)\, \dot{\kappa} + h(\kappa)\, g'(T)\, \dot{T} \end{cases} \tag{50}$$

where

$$\begin{cases} h(\kappa) = \dfrac{Q_0}{n+1}\left(\varepsilon_0 + \kappa\right)^{n+1} - \dfrac{C}{D}\left(D\kappa - exp\left(-D\kappa\right)\right) \\ g(T) = 1 - \langle \dfrac{T - T_{ref}}{T_m - T_{ref}} \rangle^{m_T} \end{cases} \tag{51}$$

* Yield function

$$f\left(\underline{\underline{\hat{\Sigma}}}, k, r\right) = \sigma_{eq}\left(\hat{\Sigma}_p, k\right) - \left[R_0 g(T) + r(\kappa, T)\right] = \sigma_v(\dot{\kappa}) \geq 0 \tag{52}$$

where

$$\begin{aligned} \sigma_{eq}\left(\hat{\Sigma}_p, k\right) &= \frac{1}{{m_0}^a}\left\{\left(|\hat{\Sigma}_1| - k\hat{\Sigma}_1\right)^a + \left(|\hat{\Sigma}_2| - k\hat{\Sigma}_2\right)^a + \left(|\hat{\Sigma}_3| - k\hat{\Sigma}_3\right)^a\right\} \\ \hat{\Sigma}_p &= eig(\underline{\underline{\hat{\Sigma}}}) \\ \underline{\underline{\hat{\Sigma}}} &= \underline{\underline{\underline{\underline{A}}}} : \left(\underline{\underline{s}} - \underline{\underline{X}}\right) \end{aligned} \tag{53}$$

* Complementary laws

$$\begin{cases} \dot{\kappa} = \langle \dfrac{f}{Y_v} \rangle^{n_v} \\ \underline{\underline{\dot{\epsilon}}}^p = \dot{\kappa}\underline{\underline{n}} \\ \underline{\underline{\dot{\alpha}}} = \underline{\underline{\dot{\epsilon}}}^p - D\dot{\kappa}\underline{\underline{\alpha}} \\ \dot{T} = \dfrac{\beta\sigma_{vm}}{\rho c}\dot{\kappa} \end{cases} \tag{54}$$

where

$$\begin{cases} \underline{\underline{n}} = \displaystyle\sum_{p=1}^{3}\left[\frac{1}{m_0^a}\left(\frac{|\hat{\Sigma}_p| - k\hat{\Sigma}_p}{\sigma_{eq}}\right)^{a-1}\left(sgn\left(\hat{\Sigma}_p\right) - k\right)\right]\underline{\underline{\underline{\underline{J}}}} : \underline{\underline{\underline{\underline{A}}}} : \left(\underline{v}_p \otimes \underline{v}_p\right) \\ \beta = \dfrac{\sigma_{eq} - r + \frac{2}{3}CD\underline{\underline{\alpha}} : \underline{\underline{\alpha}}}{\sigma_{vm}} \\ \sigma_{vm} = \sqrt{\dfrac{3}{2}\underline{\underline{s}} : \underline{\underline{s}}} \end{cases} \tag{55}$$

* Initial conditions

$$\begin{cases} \underline{\underline{\varepsilon}}^p(0) = \underline{\underline{0}} \\ \underline{\underline{X}}(0) = \underline{\underline{0}} \\ r(0) = 0 \\ T(0) = T_0 \end{cases} \tag{56}$$

* Material constants

Elasticity: $E = 110\,\mathrm{GPa}$, $\nu = 0.3$

Anisotropy (9): $a, k, A_{11}, A_{22}, A_{33}, A_{44}, A_{12}, A_{23}, A_{13}, A_{55} = A_{66} = 1$

Viscosity (2): Y_v, n_v

Hardening (6): $R_0, Q_0, \varepsilon_0, n, C, D$

Temperature (2): $m_T, T_{ref} = 25\,^\circ\mathrm{C}, T_m = 1600\,^\circ\mathrm{C}$

4. Model implementation, identification and validation

This section aims at showing the numerical procedure used to implement the material constitutive equations as a user material subroutine in a commercial finite element code (LS-DYNA) using an explicit time integration of the rate equations. The identification of the material coefficients using the commercial software Z-set is then pursued so as to check the validity of the model as well as its limitations. Finally, a validation using notched specimens is performed.

4.1. Numerical procedure

The numerical time integration of the constitutive equations starts with a finite differences scheme in the co-rotational frame. This means a push forward operation has been previously performed. The elastic strain rate is therefore

approximated as an increment between times t^i and t^{i+1} which can be decomposed in a volumetric part (not playing a role in the viscoplastic problem here defined) and a deviatoric part.

$$\begin{cases} \dot{p} = -K\dot{\varepsilon}_v + 3\alpha K\dot{T} = K\left(\dot{\varepsilon}^T - \dot{\varepsilon}_v\right) \\ \dot{\underline{\underline{s}}} = 2\mu\dot{\underline{\underline{\varepsilon}}}^e_{dev} \end{cases} \rightarrow \quad \begin{cases} \Delta p = K\left(\Delta\varepsilon^T - \Delta\varepsilon_v\right) \\ \Delta\underline{\underline{s}} = 2\mu\Delta\underline{\underline{\varepsilon}}^e_{dev} \end{cases} \tag{57}$$

where $\dot{\varepsilon}^T = 3\alpha\dot{T} = 3\alpha\left(\dot{T}_{iso} + \dot{T}_{adia}\right)$ is the thermal strain rate related to the increase in temperature (i) under isothermal conditions, i.e. a global external temperature and (ii) due to the adiabatic self-heating of the material. Hence, two thermal strain increments can be defined: $\Delta\varepsilon^T_{iso} = 3\alpha\Delta T_{iso}$ and $\Delta\varepsilon^T_{adia} = 3\alpha\Delta T_{adia}$.

The total strain increment is accordingly decomposed in an elastic, plastic and two thermal components.

$$\Delta\underline{\underline{\varepsilon}} = \Delta\underline{\underline{\varepsilon}}^e + \Delta\underline{\underline{\varepsilon}}^p + \frac{1}{3}\Delta\varepsilon^T_{iso}\underline{\underline{I}} + \frac{1}{3}\Delta\varepsilon^T_{adia}\underline{\underline{I}} \tag{58}$$

The corresponding volumetric and deviatoric parts are

$$\begin{cases} \Delta\varepsilon_v = trace\left(\Delta\underline{\underline{\varepsilon}}\right) = trace\left(\Delta\underline{\underline{\varepsilon}}^e\right) + \Delta\varepsilon^T_{iso} + \Delta\varepsilon^T_{adia} \\ \Delta\underline{\underline{\varepsilon}}_{dev} = \Delta\underline{\underline{\varepsilon}}^e_{dev} + \Delta\underline{\underline{\varepsilon}}^p_{dev} \end{cases} \tag{59}$$

The strategy used to integrate the equations is based on a two-step elastic prediction-plastic correction algorithm [79] (see Figure 17). An explicit integration of the total strain increment from the equilibrium equations is considered as the input variable in the algorithm.

The plastic correction is carried out with a direct integration of the Perzyna formulation (see [75]). The yield surface value to be used is a first order approximation based on its value at the previous increment and an estimation of its increment.

$$\dot{\kappa} = \langle\frac{f}{Y_v}\rangle^{n_v} \rightarrow \Delta\kappa = \langle\frac{f^{i+1/2}}{Y_v}\rangle^{n_v}\Delta t = \langle\frac{f^i + \frac{1}{2}\Delta f}{Y_v}\rangle^{n_v}\Delta t \tag{60}$$

In order to integrate Equation 60, an approximation of the yield surface increment is done by expanding its partial derivatives with respect to its arguments.

$$\begin{aligned}\Delta f &= \frac{\partial f}{\partial \underline{\underline{\sigma}}} : \Delta \underline{\underline{\sigma}} + \frac{\partial f}{\partial \underline{\underline{X}}} : \Delta \underline{\underline{X}} + \frac{\partial f}{\partial \kappa}\Delta\kappa + \frac{\partial f}{\partial T}\Delta T \\ &= \underline{\underline{n}} : \Delta \underline{\underline{s}}^{trial} \\ &- \left(2\mu \underline{\underline{n}} : \underline{\underline{n}} + g'\left(T^i\right) R\left(\kappa^i\right) \left.\frac{\partial T}{\partial \kappa}\right|^i + g\left(T^i\right) R'\left(\kappa^i\right) + \underline{\underline{n}} : \frac{\partial \underline{\underline{X}}}{\partial \kappa} \right) \Delta\kappa_0\end{aligned} \tag{61}$$

An initial estimation of the plastic strain increment is defined as

$$\Delta\kappa_0 = \langle \frac{f^i}{Y_v} \rangle^{n_v} \Delta t \tag{62}$$

The partial derivative of the temperature with respect to the plastic strain is obtained by using the reduced heat expression in Equation 25.

$$\left.\frac{\partial T}{\partial \kappa}\right|^i = \frac{\beta^i \sigma^i_{vm}}{\rho c} \tag{63}$$

The reason for this first order approximation is to delay instabilities as the imposed strain increments become large. Figure 16 shows a comparison between the forward Euler integration (using the yield function at the time instant t^n) and the first order approximation just described. When compared to an implicit solution, where convergence to the exact solution is presumed, the forward Euler shows instabilities for very high strain rates. Some slight oscillations can be observed on the stress-strain curve as well as some larger ones when computing the plastic strain rate. Therefore, a first-order approximation of the yield surface at the time instant $t^{n+1/2}$ provides with a much closer and more stable solution with respect to the implicit one without recurring to a computationally costly implicit loop.

Once the cumulative equivalent plastic strain κ is integrated, the rest of the state variables, i.e., the kinematic variable and the temperature can be

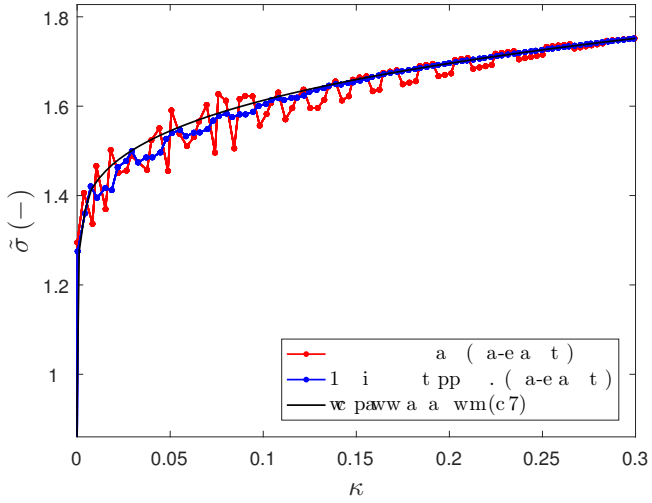

(a) Tensile stress.

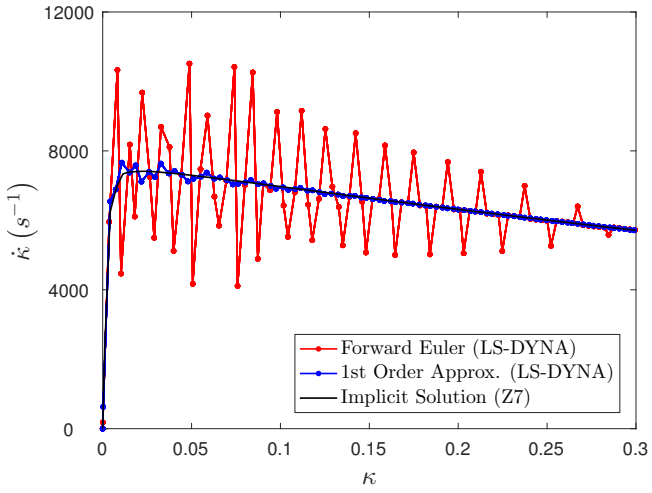

(b) Plastic Strain Rate.

Figure 16: Uniaxial tensile simulation at the element scale.

updated. A discrete approximation of Equations 45 and 48 as well as Equation 46 is considered:

$$\begin{cases} \Delta\underline{\underline{\alpha}} = \left(\underline{\underline{n}}^{trial} - \dfrac{3D}{2C}\underline{\underline{X}}^{i}\right)\Delta\kappa \\ \Delta T = \dfrac{1}{\rho c}\beta^{i}\sigma_{eq}^{i}\Delta\kappa \end{cases} \tag{64}$$

Finally the update of the stress state is performed by means of a correction where the plastic strain and thermal increment contributions are subtracted. This return algorithm uses the yield direction at the trial stress state under the assumption that a radial correction is sufficient to correct the stress.

$$\begin{cases} \Delta p = \Delta p^{trial} + K\Delta\varepsilon_{v}^{T}\underline{\underline{I}} = \Delta p^{trial} + K\alpha\Delta T\underline{\underline{I}} \\ \Delta\underline{\underline{s}} = \Delta\underline{\underline{s}}^{trial} - 2\mu\Delta\underline{\underline{\varepsilon}}_{dev}^{p} = \Delta\underline{\underline{s}}^{trial} - 2\mu\underline{\underline{n}}^{trial}\Delta\kappa \end{cases} \tag{65}$$

A summary of the numerical integration is described in the flowchart depicted in Figure 17.

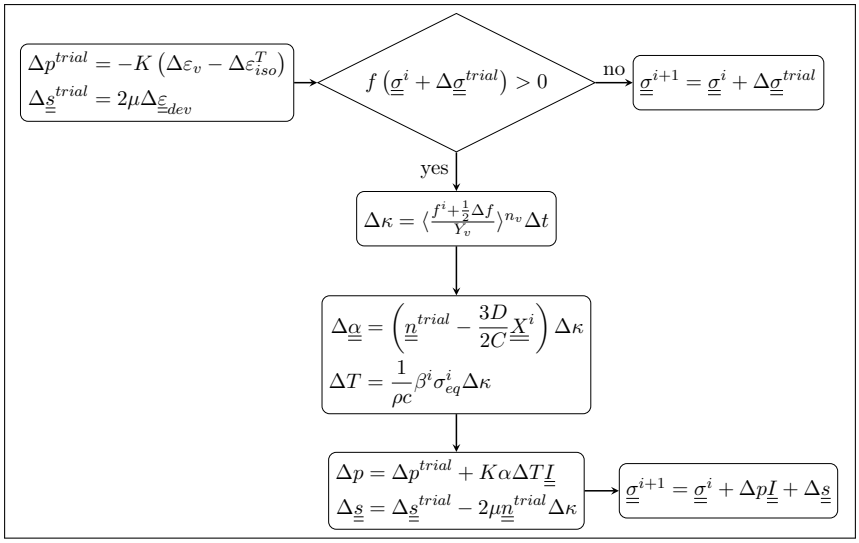

Figure 17: Numerical integration flow chart.

4.2. Model constants calibration at the volume element scale

The commercial software Z-set is chosen to carry out the identification of the material coefficients. Three stages are considered for the calibration of the material parameters: (i) 9 coefficients for the anisotropy (using the von Mises criterion as the starting point of the optimization, i.e. $a = 2$, $k = 0$ and $A_{ij} = I_{ij}$), (ii) 2 coefficients for the viscosity (once the anisotropy has been identified) and finally (iii) 7 coefficients for the strain hardening and thermal softening identification.

A volume element under uniaxial tension and compression at various strain rates along various directions is considered for the calibration. The inverse-problem identification of the material constants is performed using a gradient-based optimization method [80]. In particular, the Levenberg-Marquardt algorithm [81] is employed for the least-square minimization between the numerical and experimental results:

$$\mathcal{C}\left(\underline{p}\right) = \frac{1}{2}\sum_{i=1}^{T}\sum_{j=1}^{N} w_j \left(\sigma_j^{EXP}\left(t_i\right) - \sigma_j^{NUM}\left(\underline{p}, t_i\right)\right)^2 \tag{66}$$

where $\mathcal{C}$ is the cost function to minimize, $\underline{p}$ the set of material constants to identify, w_j a weight parameter and the subscripts i and j are used to denote different times and tests respectively. For confidentiality reason, the values of the coefficients are not given.

* Calibration of the orthotropy and strength differential related coefficients

In order to identify the anisotropy, the parameters a, k, A_{11}, A_{22}, A_{33}, A_{44}, A_{12}, A_{23} and A_{13} are fitted. For that purpose, the stress-strain tension and compression curves from the monotonic quasi-static tests run at $10^{-3}\,\mathrm{s}^{-1}$ are used. Figure 18 shows the result of such identification. The tension-compression differential is well captured as well as the orthotropy for both types of loadings.

* Calibration of the viscoplasticity related coefficients

Only the viscosity coefficients Y_v and n_v are considered in this stage. As seen with the dynamic tensile testing in Figure 5, the combined effect of self-heating induced softening and the poor camera resolution is responsible for

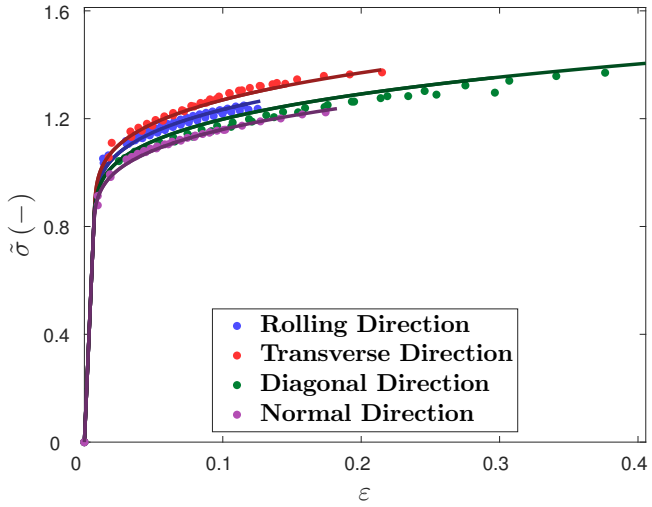

(a) Tension.

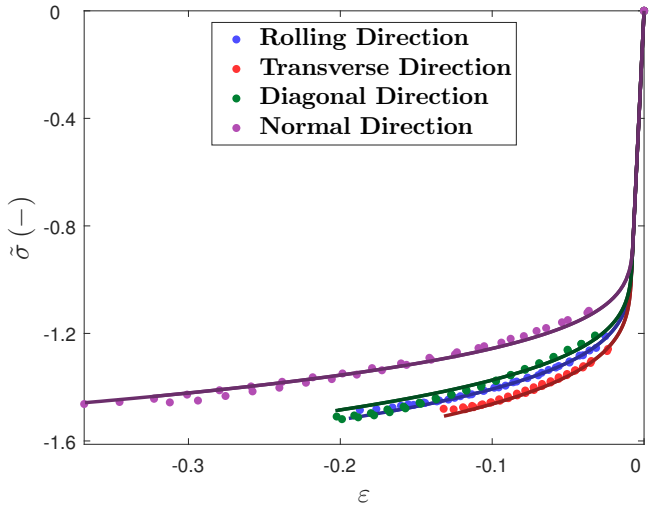

(b) Compression.

Figure 18: Stress vs strain. Tension and compression. Orthotropy related constants identification. $|\dot{\varepsilon}| \simeq 10^{-3}\,\mathrm{s}^{-1}, T = 25\,^{\circ}\mathrm{C}$

a poor measurement of the hardening curves. For this reason, the viscosity identification uses only compression stress-strain curves from monotonic quasi-static and dynamic loading plus the tension curves in the quasi-statique regime. Figure 19 shows a comparison with the identified numerical viscous model with the experimental data. The Norton law proves itself the right approximation to reproduce the overstress observed in the experiments.

Moreover, the tensile yield stress in the dynamic regime (at low strains, i.e. before the onset of self-heating softening) which is not used for identification is well estimated.

* Calibration of the strain hardening and thermal softening related coefficients

The last part of the identification is the mixed isotropic and kinematic hardening and thermal softening where parameters $R_0, K, \varepsilon_0, n, C, D, m_T$ are identified. Figure 20 summarizes the prediction capability of the model were both the monotonic and the reversed loadings are well fitted.

The material constants are summarized in Table 3.

Table 3: Material constants after calibration. Hardening coefficients Q_0, C, and Y_v are normalized with respect to R_0 (ungiven value for confidential reason), i.e. $\tilde{Q}_0 = Q_0/R_0$, $\tilde{C} = C/R_0$, $\tilde{Y}_v = Y_v/R_0$. In a same way, $\tilde{A}_{ij} = A_{ij}/A_{11}$ (with A_{11} ungiven for confidential reason) and $A_{55} = A_{66} = 1$.

E(MPa)	ν		T_{ref}(°C)	T_m(°C)	m_T		
110,000	0.3		25	1600	0.6		
$\tilde{Q}_0$	n	ε_0	$\tilde{C}$	D	$\tilde{Y}_v(s^{1/n_v})$	n_v	
0.93	0.33	1.E-08	23.22	95.3	0.16	7.0	
a	k	A_{22}	A_{33}	A_{12}	A_{23}	A_{13}	A_{44}
2	-0.17	0.994	0.983	0.327	0.260	0.242	0.710

4.3. Verification at the specimen scale

Finite Element simulations of the specimen loadings considered in the experimental campaign are herein presented to verify the performance of the model

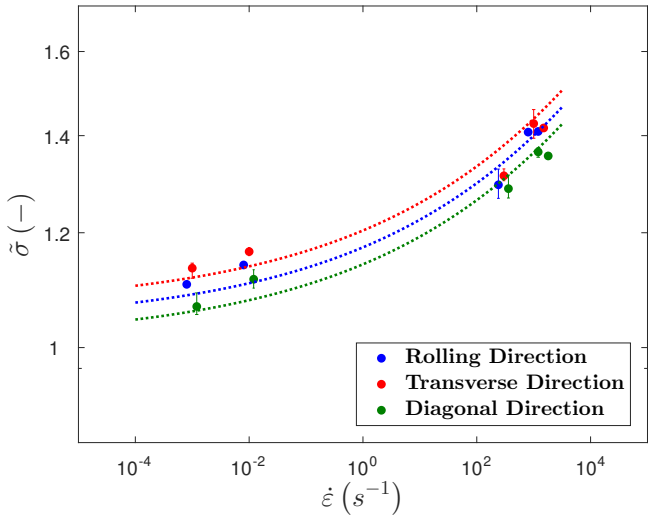

(a) Tension.

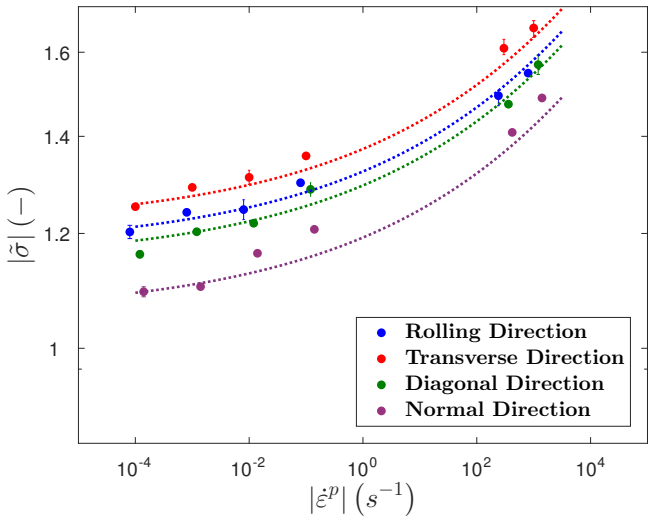

(b) Compression.

Figure 19: Stress at 2 % of plastic strain vs plastic strain rate. Tension and compression. Viscoplasticity related constants identification. $T = 25\,°\mathrm{C}$, Rolling direction RD

at the scale of a structure. The simulations used full integration 3D solid elements and some mass scaling for the explicit integration in LS-DYNA. Figure 21 shows a comparison between the numerical and the experimental results for the monotonic tension and compression specimens. For the tensile tests, the quasi-

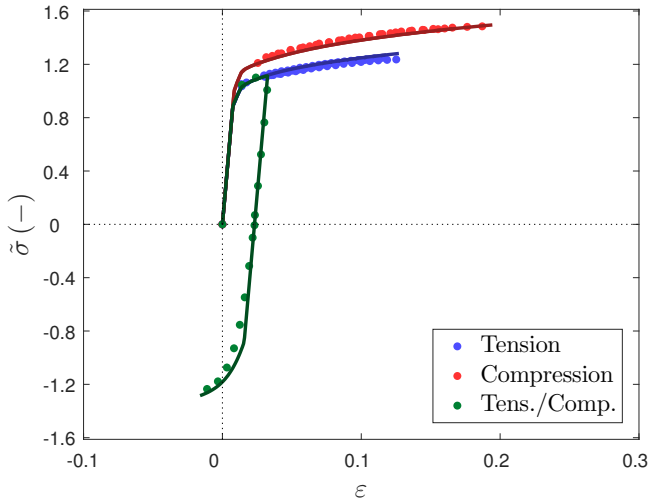

Figure 20: Stress vd strain. Results of the final identification. $\dot{\varepsilon} = 10^3\,\mathrm{s}^{-1}$, $T = 25\,^{\circ}\mathrm{C}$, Rolling direction RD.

static loading is well captured until necking. On the other hand the dynamic tensile tests are simulated by considering both isothermal and adiabatic conditions. It can be observed that with the latter, the thermal softening produces a better match with the experimental data for both tension and compression. The noise in the simulation is mainly due to the elastic waves bouncing and is highly dependent on the meshing.

The combination of a relatively low frame rate (considering the short duration of the loading) and an early spalling of the speckle painting results in an incomplete and scattered stress-strain curve in the elasto-plastic regime at high loading rates. This explains the difference of hardening between experimental (apparently lower hardening) and numerical (stronger hardening) results.

The tests on notched tensile and shear specimens with significantly different levels of stress triaxiality ratio are here compared in order to evaluate the model performance (it is noteworthy that they were not used in the calibration stage). In Figure 22, the superimposition of experimental and computed load/strain curves is shown. The verification is made by comparing the applied vs. computed load and the measured vs. computed strain (from an extensometer with

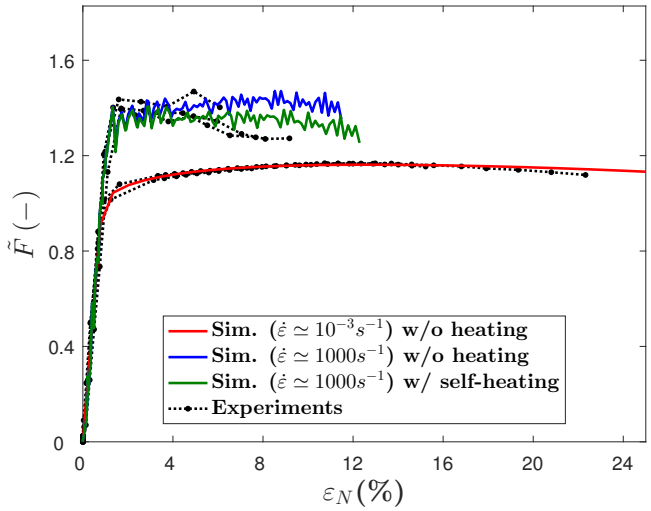

(a) Tension.

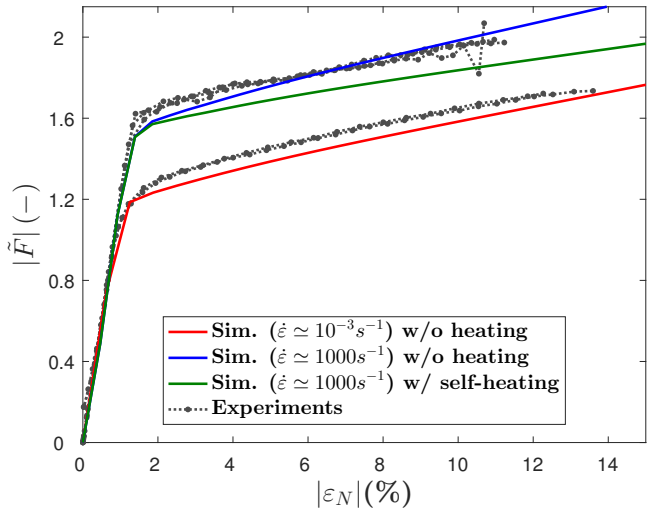

(b) Compression.

Figure 21: Load vs strain. Tension and compression. Tests within the quasi-static and dynamic regimes. $T = 25\,^{\circ}\mathrm{C}$, Transverse direction TD

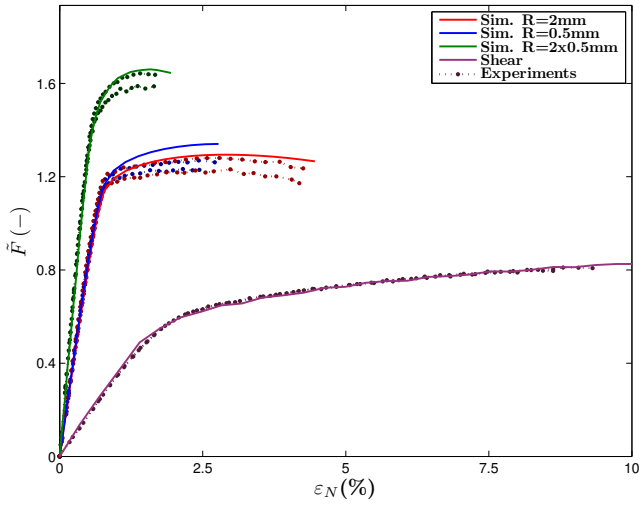

Figure 22: Load vs strain. Comparison of experimental and simulated curves for notched and shear specimens. $\dot{\varepsilon} \simeq 10^{-3}\,\mathrm{s}^{-1}$, $T = 25\,^{\circ}\mathrm{C}$, Transverse direction TD.

the same gauge length). For the three notched geometries with a positive triaxiality, the overall level of force as well as the hardening up to necking is correctly predicted with only a slight overestimation, especially for the 0.5 mm radius notch. However, this disparity remains lower than the experimental scatter. For the shear specimen, the simulation perfectly matches the experimental curve until fracture. The constitutive model seems thus to correctly model the overall behavior of the material in a wide range of stress triaxiality ratios.

Some experimental and simulated displacement or strain maps were compared for tension loading of notched specimens on which a speckle painting was applied. An example is shown in Figure 23, according to which one can conclude to a satisfactory experiment-simulation correlation.

5. Concluding remarks

An extensive experimental campaign has been performed on a Ti-6Al-4V titanium alloy, consisted in tension, compression and shear tests performed at various low and high strain rates and temperatures, and under monotonic as

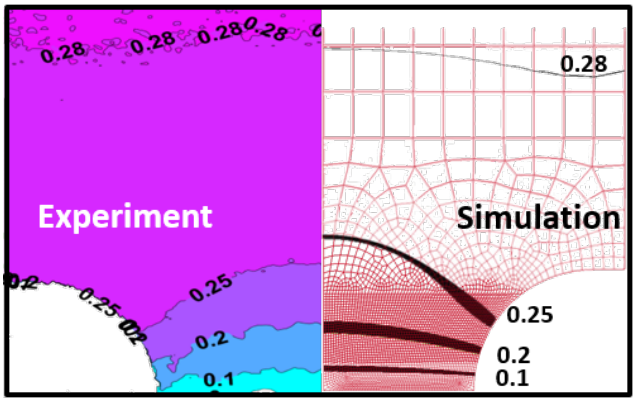

Figure 23: Experimental vs. numerical vertical displacement. Low strain rate tension loading of a notched specimen of radius 2 mm. $\dot{\varepsilon} \simeq 10^{-3}\,\mathrm{s}^{-1}$, $T = 25\,^{\circ}\mathrm{C}$, Transverse direction TD.

well as alternate loading path. Relying upon the experimental results, an advanced rate and temperature dependent constitutive model has been developed accounting for the effects of loading orientation, strength asymmetry, and nonlinear, isotropic and kinematic hardening. The model has been implemented as a user material subroutine in the commercial finite element computation code LS-DYNA and its performances have been evaluated at the structure scale considering notched and shear specimens.

Given the large number of parameters (strain rate, temperature, loading orientation, strength asymmetry, isotropic and kinematic hardening) it accounts for, this model is expected to apply to a wide range of engineering materials without significant modifications of its structure. In particular, a change in the titanium alloy thermo-mechanical treatment is expected to result in a change in some material constant values and not in the model itself.

Acknowledgment

The authors would like to acknowledge the financial support of the French Association Nationale Recherche Technologie (ANRT).

References

[1] G. Welsch, R. Boyer, E. W. Collings, Materials Properties Handbook: Titanium Alloys, Materials properties handbook, ASM International, 1993.

[2] D. G. Prakash, R. Ding, R. J. Moat, I. Jones, P. J. Withers, J. Q. da Fonseca, M. Preuss, Deformation twinning in Ti-6Al-4V during low strain rate deformation to moderate strains at room temperature, Materials Science and Engineering A 527 (21-22) (2010) 5734–5744. doi:10.1016/j.msea.2010.05.039.

[3] F. Coghe, W. Tirry, L. Rabet, D. Schryvers, P. Van Houtte, Importance of twinning in static and dynamic compression of a Ti-6Al-4V titanium alloy with an equiaxed microstructure, Materials Science and Engineering A 537 (2012) (2012) 1–10. doi:10.1016/j.msea.2011.12.047.

[4] G. Gilles, W. Hammami, V. Libertiaux, O. Cazacu, J. Yoon, T. Kuwabara, A. Habraken, L. Duchêne, Experimental characterization and elasto-plastic modeling of the quasi-static mechanical response of TA-6 V at room temperature, International Journal of Solids and Structures 48 (9) (2011) 1277–1289. doi:10.1016/J.IJSOLSTR.2011.01.011.

[5] H. P. Lee, C. Esling, H. J. Bunge, Development of the Rolling Texture in Titanium, Textures Microstruct. 7 (1988). doi:10.1155/TSM.7.317.

[6] R. Hill, A theory of the yielding and plastic flow of anisotropic metals, Proceedings of the Royal Society of London. Series A. Mathematical and Physical Sciences 193 (1033) (1948) 281–297. doi:10.1098/rspa.1948.0045.

[7] D. Mohr, M. Dunand, K. H. Kim, Evaluation of associated and non-associated quadratic plasticity models for advanced high strength steel sheets under multi-axial loading, International Journal of Plasticity 26 (7) (2010) 939–956. doi:10.1016/j.ijplas.2009.11.006.

[8] A. Taherizadeh, D. E. Green, J. Yoon, A non-associated plasticity model with anisotropic and nonlinear kinematic hardening for simulation of sheet metal forming, International Journal of Solids and Structures (2015). doi:10.1016/j.ijsolstr.2015.05.013.

[9] X. Li, C. C. Roth, D. Mohr, Machine-learning based temperature- and rate-dependent plasticity model: Application to analysis of fracture experiments on DP steel, International Journal of Plasticity (2019). doi:10.1016/j.ijplas.2019.02.012.

[10] A. Baltov, A. Sawczuk, A rule of anisotropic hardening, Acta Mechanica 1 (2) (1965) 81–92. doi:10.1007/BF01174305.

[11] J. P. Boehler, Application of Tensor Functions in Solid Mechanics, 1987. doi:10.1007/978-3-7091-2810-7_6.

[12] A. Karafillis, M. Boyce, A general anisotropic yield criterion using bounds and a transformation weighting tensor, Journal of the Mechanics and Physics of Solids 41 (12) (1993) 1859–1886. doi:10.1016/0022-5096(93)90073-O.

[13] R. T. Rockafellar, Convex analysis, Princeton, N.J. : Princeton University Press, 1970.

[14] F. Barlat, D. Lege, J. Brem, A six-component yield function for anisotropic materials, International Journal of Plasticity 7 (7) (1991) 693–712. doi:10.1016/0749-6419(91)90052-Z.

[15] F. Barlat, R. Becker, Y. Hayashida, Y. Maeda, M. Yanagawa, K. Chung, J. Brem, D. Lege, K. Matsui, S. Murtha, S. Hattori, Yielding description for solution strengthened aluminum alloys, International Journal of Plasticity 13 (4) (1997) 385–401. doi:10.1016/S0749-6419(97)80005-8.

[16] F. Barlat, J. Brem, J. Yoon, K. Chung, R. Dick, D. Lege, F. Pourboghrat, S.-H. Choi, E. Chu, Plane stress yield function for aluminum alloy

sheets—part 1: theory, International Journal of Plasticity 19 (9) (2003) 1297–1319. doi:10.1016/S0749-6419(02)00019-0.

[17] J. Yoon, F. Barlat, R. Dick, K. Chung, T. J. Kang, Plane stress yield function for aluminum alloy sheets—part II: FE formulation and its implementation, International Journal of Plasticity 20 (3) (2004) 495–522. doi:10.1016/S0749-6419(03)00099-8.

[18] G. Gilles, O. Cazacu, W. Hammami, A. Habraken, L. Duchêne, Experimental and numerical study of TA-6 V mechanical behavior in different monotonic loading conditions at room temperature, Procedia IUTAM 3 (2012) 100–114. doi:10.1016/J.PIUTAM.2012.03.008.

[19] F. Bron, J. Besson, A yield function for anisotropic materials Application to aluminum alloys, International Journal of Plasticity 20 (4-5) (2004) 937–963. doi:10.1016/J.IJPLAS.2003.06.001.

[20] M. A. Lowden, W. B. Hutchinson, Texture strengthening and strength differential in titanium-6Al-4V, Metallurgical Transactions A 6 (2) (1975) 441–448. doi:10.1007/BF02658401.

[21] W. F. Hosford, T. J. Allen, Twinning and directional slip as a cause for a strength differential effect, Metallurgical Transactions 4 (5) (1973) 1424–1425. doi:10.1007/BF02644545.

[22] O. Cazacu, F. Barlat, A criterion for description of anisotropy and yield differential effects in pressure-insensitive metals, International Journal of Plasticity 20 (11) (2004) 2027–2045. doi:10.1016/J.IJPLAS.2003.11.021.

[23] J. Yoon, Y. Lou, J. Yoon, M. V. Glazoff, Asymmetric yield function based on the stress invariants for pressure sensitive metals, International Journal of Plasticity 56 (2014) 184–202. doi:10.1016/J.IJPLAS.2013.11.008.

[24] A. S. Khan, S. Yu, H. Liu, Deformation induced anisotropic responses of Ti–6Al–4V alloy Part II: A strain rate and temperature dependent

anisotropic yield criterion, International Journal of Plasticity 38 (2012) 14–26. doi:10.1016/J.IJPLAS.2012.03.013.

[25] O. Cazacu, B. Plunkett, F. Barlat, Orthotropic yield criterion for hexagonal closed packed metals, International Journal of Plasticity 22 (7) (2006) 1171–1194. doi:10.1016/j.ijplas.2005.06.001.

[26] V. Tuninetti, A. Habraken, Impact of anisotropy and viscosity to model the mechanical behavior of Ti–6Al–4V alloy, Materials Science and Engineering: A 605 (2014) 39–50. doi:10.1016/J.MSEA.2014.03.009.

[27] V. Tuninetti, G. Gilles, O. Milis, T. Pardoen, A. Habraken, Anisotropy and tension–compression asymmetry modeling of the room temperature plastic response of Ti–6Al–4V, International Journal of Plasticity 67 (2015) 53–68. doi:10.1016/J.IJPLAS.2014.10.003.

[28] D. Steglich, X. Tian, J. Besson, Mechanism-based modelling of plastic deformation in magnesium alloys, European Journal of Mechanics, A/Solids 55 (2016) 289–303. doi:10.1016/j.euromechsol.2015.09.011.

[29] F. Barlat, J. J. Gracio, M.-G. Lee, E. F. Rauch, G. Vincze, An alternative to kinematic hardening in classical plasticity, International Journal of Plasticity 27 (9) (2011) 1309–1327. doi:10.1016/J.IJPLAS.2011.03.003.

[30] N. Manopulo, C. Raemy, P. Hora, A flexible modelling approach for capturing plastic anisotropy and strength differential effects exhibited by commercially pure titanium, International Journal of Solids and Structures 151 (2018) 91–98. doi:10.1016/j.ijsolstr.2017.05.027.

[31] P. Longère, A.-G. Geffroy, B. Leblé, A. Dragon, Modeling the Transition between Dense Metal and Damaged (Microporous) Metal Viscoplasticity, International Journal of Damage Mechanics 21 (7) (2012) 1020–1063. doi:10.1177/1056789511427472.

[32] L. Zhonghua, G. Haicheng, Bauschinger effect and residual phase stresses in two ductile-phase steels: Part I. The influence of phase stresses on the

Bauschinger effect, Metallurgical Transactions A 21 (2) (1990) 717–724. doi:10.1007/BF02671942.

[33] L. Zhonghua, G. Haicheng, Bauschinger effect and residual phase stresses in two ductile-phase steels: Part II. The effect of microstructure and mechanical properties of the constituent phases on Bauschinger effect and residual phase stresses, Metallurgical Transactions A 21 (2) (1990) 725–732. doi:10.1007/BF02671943.

[34] A. L. Helbert, X. Feaugas, M. Clavel, The influence of the back stress (X) and the hardening rate (dX/x epsilon(peq)) on void nucleation in alpha/beta titanium alloys, Journal De Physique Iv 6 (C6) (1996) 101–111.

[35] J. Lemaitre, J. Chaboche, Mechanics of Solid Materials, Cambridge University Press, 1994. doi:10.1017/CBO9781139167970.

[36] P. J. Armstrong, C. O. Frederick, A mathematical representation of the multiaxial Bauschinger effect, Vol. 731, Central Electricity Generating Board [and] Berkeley Nuclear Laboratories˜..., 1966.

[37] J. Chaboche, Time-independent constitutive theories for cyclic plasticity, International Journal of Plasticity 2 (2) (1986) 149–188. doi:10.1016/0749-6419(86)90010-0.

[38] B. Chun, J. Jinn, J. Lee, Modeling the Bauschinger effect for sheet metals, part I: theory, International Journal of Plasticity 18 (5-6) (2002) 571–595. doi:10.1016/S0749-6419(01)00046-8.

[39] J. Carbonnière, S. Thuillier, F. Sabourin, M. Brunet, P. Y. Manach, Comparison of the work hardening of metallic sheets in bending-unbending and simple shear, International Journal of Mechanical Sciences 51 (2) (2009) 122–130. doi:10.1016/j.ijmecsci.2008.12.006.

[40] S. Zang, C. Guo, S. Thuillier, M. Lee, A model of one-surface cyclic plasticity and its application to springback prediction, International Journal

of Mechanical Sciences 53 (6) (2011) 425–435. doi:10.1016/J.IJMECSCI.2011.03.005.

[41] K. Minnaar, M. Zhou, An analysis of the dynamic shear failure resistance of structural metals, Journal of the Mechanics and Physics of Solids 46 (10) (1998) 2155–2170. doi:10.1016/s0022-5096(98)00020-9.

[42] G. R. Johnson, W. H. Cook, A constitutive model and data for metals subjected to large strains, high strain rates and high temperatures, in: Proceedings 7th International Symposium on Ballistics, The Hague, 1983, pp. 541–547.

[43] A. S. Khan, Y. Sung Suh, R. Kazmi, Quasi-static and dynamic loading responses and constitutive modeling of titanium alloys, International Journal of Plasticity 20 (12) (2004) 2233–2248. doi:10.1016/J.IJPLAS.2003.06.005.

[44] P. Longère, A. Dragon, Description of shear failure in ductile metals via back stress concept linked to damage-microporosity softening, Engineering Fracture Mechanics 98 (2013) 92–108. doi:10.1016/J.ENGFRACMECH.2012.11.009.

[45] S. Seo, O. Min, H. Yang, Constitutive equation for Ti-6Al-4V at high temperatures measured using the SHPB technique, International Journal of Impact Engineering 31 (6) (2005) 735–754. doi:10.1016/j.ijimpeng.2004.04.010.

[46] J. Galán López, P. Verleysen, J. Degrieck, Thermal Effects During Tensile Deformation of Ti-6Al-4V at Different Strain Rates, Strain 49 (2013). doi:10.1111/str.12042.

[47] D. Macdougall, J. Harding, A constitutive relation and failure criterion for Ti6Al4V alloy at impact rates of strain, Journal of the Mechanics and Physics of Solids 47 (5) (1999) 1157–1185. doi:10.1016/S0022-5096(98)00086-6.

[48] P. Longère, A. Dragon, Dynamic vs. quasi-static shear failure of high strength metallic alloys: Experimental issues, Mechanics of Materials 80 (PB) (2015) 203–218. doi:10.1016/j.mechmat.2014.05.001.

[49] T. Tancogne-Dejean, C. C. Roth, U. Woy, D. Mohr, Probabilistic fracture of Ti-6Al-4V made through additive layer manufacturing, International Journal of Plasticity 78 (2016) 145–172. doi:10.1016/j.ijplas.2015.09.007.

[50] A. S. Khan, R. Kazmi, B. Farrokh, Multiaxial and non-proportional loading responses, anisotropy and modeling of Ti–6Al–4V titanium alloy over wide ranges of strain rates and temperatures, International Journal of Plasticity 23 (6) (2007) 931–950. doi:10.1016/J.IJPLAS.2006.08.006.

[51] M. Zhang, J. Zhang, D. McDowell, Microstructure-based crystal plasticity modeling of cyclic deformation of Ti–6Al–4V, International Journal of Plasticity 23 (8) (2007) 1328–1348. doi:10.1016/J.IJPLAS.2006.11.009.

[52] J. Mayeur, D. McDowell, A three-dimensional crystal plasticity model for duplex Ti–6Al–4V, International Journal of Plasticity 23 (9) (2007) 1457–1485. doi:10.1016/J.IJPLAS.2006.11.006.

[53] K. Le Biavant, S. Pommier, C. Prioul, Local texture and fatigue crack initiation in a Ti-6Al-4V titanium alloy, Fatigue & Fracture of Engineering Materials & Structures 25 (2002) 527–545. doi:10.1046/j.1460-2695.2002.00480.x.

[54] C. C. Roth, D. Mohr, Determining the strain to fracture for simple shear for a wide range of sheet metals, International Journal of Mechanical Sciences 149 (2018) 224–240. doi:10.1016/J.IJMECSCI.2018.10.007.

[55] M. Dunand, G. Gary, D. Mohr, Load-Inversion Device for the High Strain Rate Tensile Testing of Sheet Materials with Hopkinson Pressure Bars, Experimental Mechanics 53 (2013). doi:10.1007/s11340-013-9712-y.

[56] C. C. Roth, G. Gary, D. Mohr, Compact SHPB System for Intermediate and High Strain Rate Plasticity and Fracture Testing of Sheet Metal, Experimental Mechanics 55 (9) (2015) 1803–1811. doi:10.1007/s11340-015-0061-x.

[57] H. Zhao, G. Gary, On the use of SHPB techniques to determine the dynamic behavior of materials in the range of small strains, International Journal of Solids and Structures 33 (23) (1996) 3363–3375. doi:10.1016/0020-7683(95)00186-7.

[58] J. Dickson, J. Boutin, L. Handfield, A comparison of two simple methods for measuring cyclic internal and effective stresses, Materials Science and Engineering 64 (1) (1984) L7–L11. doi:10.1016/0025-5416(84)90083-1.

[59] P. Longère, Respective/combined roles of thermal softening and dynamic recrystallization in adiabatic shear banding initiation, Mechanics of Materials 117 (2018) 81–90. doi:10.1016/J.MECHMAT.2017.10.003.

[60] G. I. Taylor, H. Quinney, The latent energy remaining in a metal after cold working, Proceedings of the Royal Society of London. Series A, Containing Papers of a Mathematical and Physical Character 143 (849) (1934) 307–326.

[61] J. Mason, A. Rosakis, G. Ravichandran, On the strain and strain rate dependence of the fraction of plastic work converted to heat: an experimental study using high speed infrared detectors and the kolsky bar, Mechanics of Materials 17 (2) (1994) 135 – 145. doi:https://doi.org/10.1016/0167-6636(94)90054-X.
URL http://www.sciencedirect.com/science/article/pii/016766369490054X

[62] E. H. Lee, D. T. Liu, Finite-strain elastic—plastic theory with application to plane-wave analysis, Journal of applied physics 38 (1) (1967) 19–27.

[63] E. Lee, Elastic-Plastic Deformation at Finite Strains, Journal of Applied Mechanics 36 (1) (1969) 1–6. doi:10.1115/1.3564580.

[64] P. Longère, A. Dragon, H. Trumel, T. de Resseguier, X. Deprince, E. Petitpas, Modelling adiabatic shear banding via damage mechanics approach, Vol. 55, 2003.

[65] B. Schieck, H. Stumpf, The appropriate corotational rate, exact formula for the plastic spin and constitutive model for finite elastoplasticity, International Journal of Solids and Structures 32 (24) (1995) 3643–3667. doi:10.1016/0020-7683(95)00007-W.

[66] J. Mandel, Equations constitutives et directeurs dans les milieux plastiques et viscoplastiques, International Journal of Solids and Structures 9 (6) (1973) 725–740. doi:10.1016/0020-7683(73)90120-0.

[67] T. Hughes, J. Winget, Finite rotation effects in numerical integration of rate constitutive equations arising in large-deformation analysis, International Journal for Numerical Methods in Engineering 15 (12) (1980) 1862–1867. doi:10.1002/nme.1620151210.

[68] P. Longère, Numerical integration of rate constitutive equations in presence of large strains and rotations, Mechanics Research Communications 95 (2019) 61–66. doi:10.1016/J.MECHRESCOM.2018.12.001.

[69] B. Halphen, Q. S. Nguyen, Sur les Matériaux Standard Généralisés, Journal de Mécanique 14 (1) (1975) 39–63.

[70] P. Longère, A. Dragon, Inelastic heat fraction evaluation for engineering problems involving dynamic plastic localization phenomena, Journal of Mechanics of Materials and Structures - J MECH MATER STRUCT 4 (2009) 319–349. doi:10.2140/jomms.2009.4.319.

[71] P. Longère, A. Dragon, Evaluation of the inelastic heat fraction in the context of microstructure-supported dynamic plasticity modelling, Inter-

national Journal of Impact Engineering 35 (9) (2008) 992–999. doi:10.1016/J.IJIMPENG.2007.06.006.

[72] W. F. Hosford, A Generalized Isotropic Yield Criterion, Journal of Applied Mechanics 39 (2) (1972) 607–609. doi:10.1115/1.3422732.
URL https://doi.org/10.1115/1.3422732

[73] J. B. Stewart, O. Cazacu, Analytical yield criterion for an anisotropic material containing spherical voids and exhibiting tension–compression asymmetry, International Journal of Solids and Structures 48 (2) (2011) 357–373. doi:10.1016/J.IJSOLSTR.2010.10.009.

[74] F. Norton, The Creep of Steel at High Temperatures, McGraw-Hill Book Company, 1929.

[75] P. Perzyna, Fundamental Problems in Viscoplasticity, Advances in Applied Mechanics 9 (1966) 243–377. doi:10.1016/S0065-2156(08)70009-7.

[76] C. C. Roth, D. Mohr, Ductile fracture experiments with locally proportional loading histories, International Journal of Plasticity 79 (2016) 328–354. doi:10.1016/J.IJPLAS.2015.08.004.

[77] G. Vadillo, R. Zaera, J. Fernández-Sáez, Consistent integration of the constitutive equations of Gurson materials under adiabatic conditions, Computer Methods in Applied Mechanics and Engineering 197 (13-16) (2008) 1280–1295. doi:10.1016/J.CMA.2007.11.008.

[78] P. Rosakis, A. Rosakis, G. Ravichandran, J. Hodowany, A thermodynamic internal variable model for the partition of plastic work into heat and stored energy in metals, Journal of the Mechanics and Physics of Solids 48 (3) (2000) 581 – 607. doi:https://doi.org/10.1016/S0022-5096(99)00048-4.
URL http://www.sciencedirect.com/science/article/pii/S0022509699000484

[79] J. Simo, T. Hughes, Computational Inelasticity, 1998. arXiv:1406.6401, doi:10.1016/j.camwa.2013.03.019.

[80] A. Andrade-Campos, S. Thuillier, P. Pilvin, F. Teixeira-Dias, On the determination of material parameters for internal variable thermoelastic–viscoplastic constitutive models, International Journal of Plasticity 23 (8) (2007) 1349–1379. doi:10.1016/J.IJPLAS.2006.09.002.

[81] D. W. Marquardt, An algorithm for least-squares estimation of nonlinear parameters, Journal of the society for Industrial and Applied Mathematics 11 (2) (1963) 431–441.